Fig. 2. Representative features of tissue-infiltrating FOXP3+, CD4+, or CD8+ T lymphocytes. CH (*A-D*), AH (*E-H*), early HCC (*I-L*), and MD HCC (*M-P*) by HE staining (*A, E, I,* and *M*) and immunostaining for FOXP3 (*B, F, J,* and *N*), CD4 (*C, G, K,* and *O*), and CD8 (*D, H, L,* and *P*).
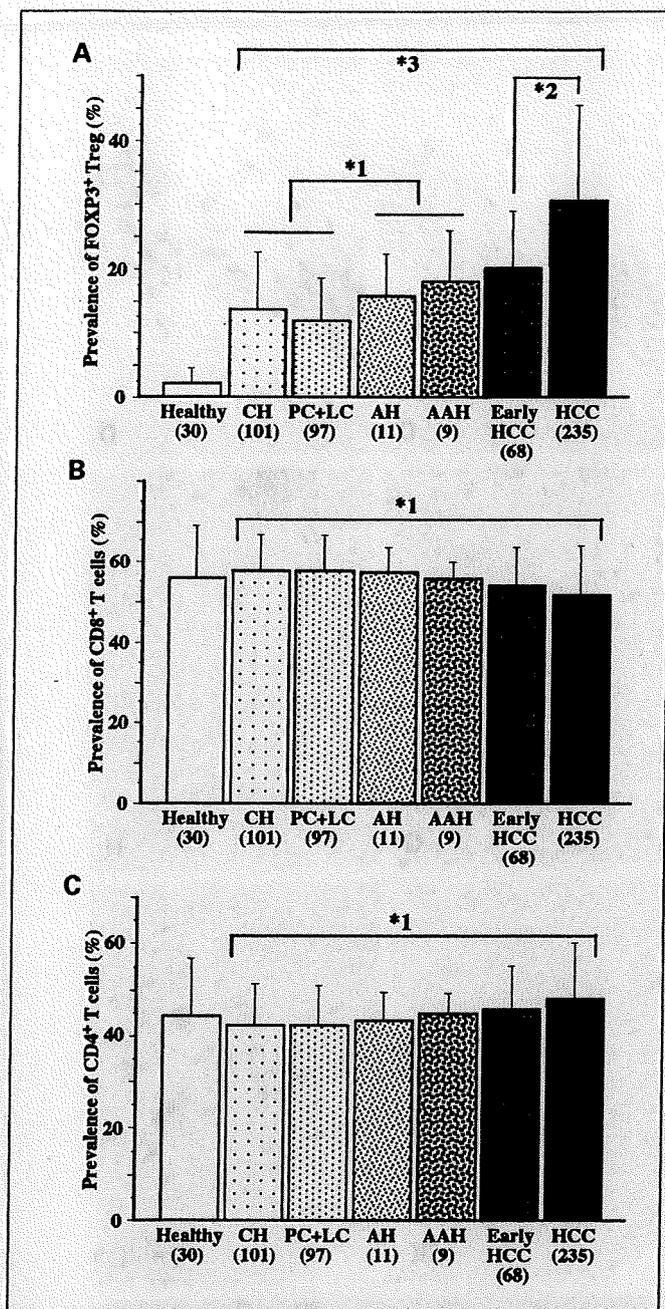
Fig. 3. Increased population of Tregs and decreased population of CD8+ T cells in tumor stroma corresponding to the progression of multistage hepatocarcinogenesis. Prevalence of Tregs among CD4+ T cells (A), prevalence of CD8+ T cells among total T cells (B), and prevalence of CD4+ T cells among total T cells (C) in HCC, its precursor lesions, and nontumorous liver. Number of cases tested in parentheses; Thin bars, SD. A, *1, P = 0.038; *2, P < 0.001; *3, P < 0.001 (Kruskal-Wallis test). B and C, *1, P < 0.001 (Kruskal-Wallis test).

was significantly higher in primary HCC than in IM (P = 0.003; Fig. 4A). Also, the prevalence of Tregs in primary hepatic adenocarcinoma was higher than that in metastatic hepatic adenocarcinoma (P = 0.020; Fig. 4A). The prevalence of CD8+ T cells was comparable between primary and metastatic tumors.

Hepatitis viral infection and antitumor host immune response. HBV or HCV infection is a risk factor for the development of HCC (2), and it is also reported that these chronic viral infections suppress the host immune response (2).

Some investigators have suggested that HCV infection increases ICC development, although this remains to be proven (34). The prevalence of Tregs in nontumorous liver of patients infected with HBV or HCV was significantly higher than in healthy liver (Fig. 4B), even in patients who were in the so-called "carrier" stage, with infection but no detectable manifestations or histologic changes. To investigate whether Tregs affected the development of primary liver tumors, we compared the prevalence of Tregs in nontumorous areas of liver bearing HCC, ICC, or metastatic liver adenocarcinoma among patients with and without hepatitis viral infection. The prevalence of Tregs in nontumorous liver bearing HCC or ICC without any HBV or HCV infection was apparently higher than that in healthy liver (versus HCC, P < 0.001; versus ICC, P < 0.001; Fig. 4B). In contrast, the prevalence of Tregs in nontumorous liver bearing HCC or ICC with HBV or HCV infection was slightly, but not significantly, higher than that in liver bearing no primary liver tumor with hepatitis virus infection (Fig. 4B). These findings suggest that a further increase of Treg infiltration in nontumorous liver with hepatitis virus infection is not closely correlated with the development of primary liver tumors. An interesting observation was that the prevalence of Tregs in nontumorous liver bearing HCC without HBV or HCV infection was higher than that in healthy liver, and was slightly lower than that in HBV-infected liver (Fig. 4B and C). The prevalence of Tregs in liver infected with HCV was higher than that in liver with HBV infection (P = 0.016), and
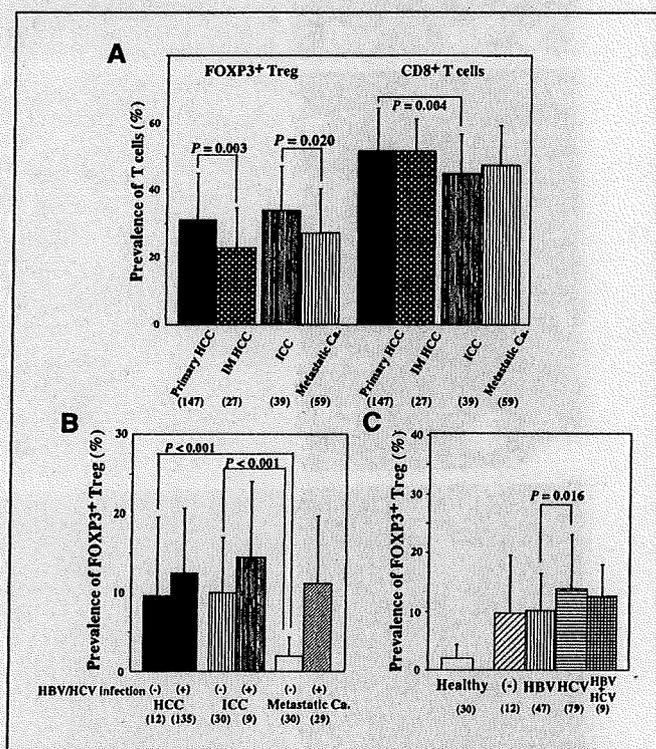

Fig. 4. A, prevalence of T cells in primary liver cancer (HCC and ICC) and metastatic HCC (IM) and adenocarcinoma from colon cancer (metastatic ca.). Left and right columns, the prevalence of Tregs and CD8+ T cells, respectively. Number of cases tested are in parentheses. B, prevalence of Tregs in nontumorous liver of patients bearing HCC, ICC, or metastatic liver cancer, with or without HBV or HBC infection. Number of cases tested in parentheses. C, prevalence of Tregs in nontumorous liver of patients bearing HCC. Prevalence of Tregs in nontumorous liver with or without (−) hepatitis B and/or C viral infection were significantly higher than that in healthy controls. Number of cases tested in parentheses.

that in both HBV- and HCV-infected liver was intermediate between that in HBV- and HCV-infected liver. These observations were also recognized in patients with ICC (data not shown).

Discussion

Tumor-infiltrating lymphocytes represent the host immune response to a tumor, and include CD8$^+$ cytotoxic T cells and natural killer cells as positive responders and Tregs as immunosuppressors. There has been no large-scale or clinicopathologic study of Tregs in HCC and tumor-infiltrating lymphocytes in hepatocarcinogenesis. In the present study, we investigated the relationship between host immune response and hepatocarcinogenesis, focusing especially on Treg infiltration. First, we showed the clinicopathologic significance of Tregs among CD4$^+$ T cells infiltrating advanced HCC based on the following findings: (*a*) the prevalence of Tregs in HCC (n = 235) was significantly higher ($P < 0.001$) than that in nontumorous liver (n = 248), which included healthy liver, NCH, CH, PC, and LC. (*b*) Patients with HCC in the high-Treg group showed a significantly lower survival ratio. Both overall survival (log-rank test, P = 0.007) and disease-free survival (log-rank test, P = 0.015) were lower than for patients with HCC belonging to the low-Treg group. (*c*) Multivariate analysis revealed that the prevalence of tumor-infiltrating Tregs was an independent prognostic factor, along with Child-Pugh classification and presence of VP, for overall survival and that the prevalence of tumor-infiltrating Tregs and that of IM were independent prognostic factors for disease-free survival. (*d*) The prevalence of tumor-infiltrating Tregs was increased in poorly differentiated HCC (Kruskal-Wallis test; $P < 0.001$). In addition, we found that the prevalence of tumor-infiltrating Tregs increased in a stepwise manner (Kruskal-Wallis test, $P < 0.001$), whereas the prevalence of CD8$^+$ T cells decreased (Kruskal-Wallis test, $P < 0.001$) during the progression of hepatocarcinogenesis. These findings suggest that Treg infiltration was closely correlated with the progression of neoplastic cells in hepatocarcinogenesis. Furthermore, we showed that the prevalence of Tregs was increased in nontumorous liver tissue from patients with primary hepatic tumors, regardless of the presence of hepatitis virus infection or histopathologically evident hepatitis or liver cirrhosis. This indicates that primary hepatic tumors develop in liver, in which Tregs show marked infiltration and immune reactivity is suppressed. This is the first report to show that infiltration of Tregs is closely correlated with the development and progression of hepatocarcinogenesis, and that the prevalence of Tregs is a useful prognostic factor in patients with HCC.

It was reported previously that CD8$^+$ T cells infiltrating tumors are associated with good prognosis (8, 9), and that tumor-infiltrating Treg is increased in a variety of tumors (21–28). A few studies have also investigated the clinicopathologic significance of Treg infiltration (23–25), but conclusions about its correlation with prognosis were contradictory. Marked infiltration of Tregs in cancer stroma was reported to be an unfavorable prognostic factor in ovarian (23) and pancreatic (25) cancers, and was associated with control of tumor progression in head and neck cancers (24). No prognostic influence of Tregs was found in anal squamous cell carcinomas (35). In the present study, using multivariate analyses, we

showed that the prevalence of Tregs in HCC was significantly correlated with both overall survival and disease-free survival. A high prevalence of Tregs was closely correlated only with histologic grade among a number of clinicopathologic variables. These findings indicate that the prevalence of tumor-infiltrating FOXP3$^+$ Tregs can be an independent prognostic factor for patients with HCC. In addition to the prevalence of Tregs, our multivariate analysis revealed that among 15 prognostic factors, Child-Pugh classification and the presence of VP and IM were independent indicators of unfavorable overall and disease-free survival, respectively, consistent with previous studies (36, 37). In contrast, infiltration of CD8$^+$ T cells as well as perforin-positive cells (data not shown) in HCC was found to have no prognostic significance. A positive prognostic effect of infiltrating CD8$^+$ T cells has been reported in various solid cancers such as colorectal (8) and ovarian (9) cancer. Only patients bearing HCC with exceptionally marked infiltration of CD8$^+$ T cells were reported to have a good prognosis (10). It is interesting that a negative prognostic effect of CD8$^+$ T cell infiltration has been observed in virus-related tumors, including EB virus–associated nasopharyngeal carcinomas (38) and human papilloma virus–associated anal carcinomas (35). This effect observed in other tumors was not observed in HCC, even though HCC is closely associated with hepatitis virus infection, and might be attributable to an organ-specific immune response.

In established HCC, Treg infiltration might play an important role in tumor progression and clinical behavior by modifying the host immune response. Furthermore, our data showed that the prevalence of Tregs increased in a stepwise manner from viral hepatitis containing CH, PC, and LC, to precursor lesions of AH and AAH, early HCC, and advanced HCC, indicating that Treg infiltration was closely involved in the progression of hepatocarcinogenesis ($P < 0.001$; Fig. 3A). It has been suggested that Tregs suppress the immune response through cell contact–dependent (12–14) or cell contact–independent mechanisms (15, 16), and that immune suppression occurs in several steps (12, 14, 16). Various immune cells could be the targets of Treg suppression, such as CD8$^+$ T cells, CD4$^+$CD25$^-$ T cells, B cells, natural killer cells, natural killer T-cells, and dendritic cells (12, 14, 16, 39, 40). In this study, the prevalence of CD8$^+$ tumor-infiltrating lymphocytes was found to decrease significantly during hepatocarcinogenesis ($P < 0.001$; Fig. 3B), and this was inversely correlated with Treg infiltration. The group of patients with advanced HCC showing marked Treg infiltration showed a tendency to have a lower prevalence of CD8$^+$ tumor-infiltrating lymphocytes (Table 2A). Thus, it is possible that Tregs contribute to reducing the infiltration of CD8$^+$ T cells during hepatocarcinogenesis. Unitt et al. reported that Tregs isolated from advanced HCC suppressed the proliferation and perforin expression of autologous circulating CD8$^+$ T cells (27).

Persistent viral infection requires host immune suppression. CD4$^+$CD25$^+$ Tregs have been reported to be linked to the chronicity and progression of viral hepatitis in patients with HBV or HCV infection by down-regulating the hepatitis virus-specific T cell response (41–43). Our present observations confirm marked infiltration of Tregs in the liver of patients infected with HBV or HCV. Regardless of the presence of hepatitis virus infection and histopathologic changes indicative of hepatitis, the prevalence of Tregs in nontumorous liver tissue

of patients bearing HCC was significantly higher than that in healthy liver, but was slightly lower than that in liver with viral hepatitis. It has been suggested that even in patients with HCC of unknown etiology, immunosuppression might have started in the liver before tumor development. In patients with primary hepatic adenocarcinoma, ICC, the prevalence of FOXP3^{+} Tregs in nontumorous liver without viral infection was also higher than that in healthy liver. These findings suggest that primary hepatic tumors can develop in the liver with a certain degree of Treg infiltration. A subsequent increase of Treg infiltration seemed to accelerate the development of hepatic tumors in patients infected with hepatitis virus, but not to a significant degree. Further studies will be necessary to clarify the threshold of Treg prevalence at which the risk of hepatic tumor development becomes high. The prevalence of Tregs in primary hepatic tumors, both HCC and adenocarcinoma, was signifi-cantly higher than that in metastatic hepatic tumors with the corresponding histology. These findings support the hypothesis that the development and progression of primary hepatic tumors involves high accumulation of Tregs.

In conclusion, our data suggest that Tregs play a role in controlling the immune response to HCC from the precursor stage to established cancer, and also that primary hepatic cancers might develop in liver that is immunosuppressed by marked infiltration of Tregs, regardless of the presence of hepatitis viral infection. A high prevalence of Tregs seems to be an indicator of poor prognosis.

Acknowledgments

References

1. Llovet JM, Burroughs A, Bruix J. Hepatocellular carcinoma. Lancet 2003;362:1907–17.
2. Kao JH, Chen DS. Overview of hepatitis B and C viruses. Infectious causes of Cancer. In: Goedert JJ, editor. New Jersey: Humana Press; 2000.
3. Ueno Y, Moriyama M, Uchida T, Arakawa Y. Irregular regeneration of hepatocytes is an important factor in the hepatocarcinogenesis of liver disease. Hepatology 2001;33:357–62.
4. Tsuda H, Hirohashi S, Shimosato Y, Terada M, Hasegawa H. Clonal origin of atypical adenomatous hyperplasia of the liver and clonal identity with hepatocellular carcinoma. Gastroenterology 1988;95:1664–6.
5. Sakamoto M, Hirohashi S, Shimosato Y. Early stages of multistep hepatocarcinogenesis: adenomatous hyperplasia and early hepatocellular carcinoma. Hum Pathol 1991;22:172–8.
6. Saito Y, Kanai Y, Sakamoto M, Saito H, Ishii H, Hirohashi S. Expression of mRNA for DNA methyltransferases and methyl-CpG-binding proteins and DNA methylation status on CpG islands and pericentromeric satellite regions during human hepatocarcinogenesis. Hepatology 2001;33:561–8.
7. Chuma M, Sakamoto M, Yamazaki K, et al. Expression profiling in multistage hepatocarcinogenesis: identification of HSP70 as a molecular marker of early hepatocellular carcinoma. Hepatology 2003;37:198–207.
8. Zhang L, Conejo-Garcia JR, Katsaros D, et al. Intratumoral T cells, recurrence, and survival in epithelial ovarian cancer. N Engl J Med 2003;348:203–13.
9. Naito Y, Saito K, Shiiba K, et al. CD8^{+} T cells infiltrated within cancer cell nests as a prognostic factor in human colorectal cancer. Cancer Res 1998;58:3491–4.
10. Wada Y, Nakashima O, Kutami R, Yamamoto O, Kojiro M. Clinicopathological study on hepatocellular carcinoma with lymphocytic infiltration. Hepatology 1998;27:407–14.
11. Nakamoto Y, Suda T, Momoi T, Kaneko S. Different procarcinogenic potentials of lymphocyte subsets in a transgenic mouse model of chronic hepatitis B. Cancer Res 2004;64:3326–33.
12. Sakaguchi S. Regulatory T cells: key controllers of immunologic self-tolerance. Cell 2000;101:455–8.
13. Dieckmann D, Plottner H, Berchtold S, Berger T, Schuler G. Ex vivo isolation and characterization of CD4^{+}CD25^{+} T cells with regulatory properties from human blood. J Exp Med 2001;193:1303–10.
14. Shevach EM. CD4^{+}CD25^{+} suppressor T cells: more questions than answers. Nat Rev Immunol 2002;2:389–400.
15. Chen ML, Pittet MJ, Gorelik L, et al. Regulatory T cells suppress tumor-specific CD8 T cell cytotoxicity through TGF-b signals in vivo. Proc Natl Acad Sci U S A 2005;102:419–24.

16. von Boehmer H. Mechanisms of suppression by suppressor T cells. Nat Immunol 2005;6:338–44.
17. Fontenot JD, Rudensky AY. A well adapted regulatory contrivance: regulatory T cell development and the forkhead family transcription factor Foxp3. Nat Immunol 2005;6:331–7.
18. Shimizu JS, Yamazaki S, Sakaguchi S. Induction of tumor immunity by removing CD25^{+}CD4^{+} T cells: a common basis between tumor immunity and autoimmunity. J Immunol 1999;163:5211–8.
19. Onizuka SI, Tawara J, Shimizu J, Sakaguchi S, Fujita T, Nakayama E. Tumor rejection by in vivo administration of anti-CD25 (interleukin-2 receptor a) monoclonal antibody. Cancer Res 1999;59:3128–33.
20. Nishikawa H, Kato T, Tawara I, et al. Accelerated chemically induced tumor development mediated by CD4^{+}CD25^{+} regulatory T cells in wild-type hosts. Proc Natl Acad Sci U S A 2005;102:9253–7.
21. Woo EY, Chu CS, Goletz TJ, et al. Regulatory CD4^{+}CD25^{+} T cells in tumors from patients with early-stage non-small lung cancer and late-stage ovarian cancer. Cancer Res 2001;61:4766–72.
22. Liyanage UK, Moore TT, Joo HG, et al. Prevalence of regulatory T cells is increased in peripheral blood and tumor microenvironment of patients with pancreas or breast adenocarcinoma. J Immunol 2002;169:2756–61.
23. Curiel TJ, Coukos G, Zou L, et al. Specific recruitment of regulatory T cells in ovarian carcinoma fosters immune privilege and predicts reduced survival. Nat Med 2004;10:942–9.
24. Badoual C, Hans S, Rodriguez J, et al. Prognostic value of tumor-infiltrating CD4^{+} T-cell subpopulations in head and neck cancers. Clin Cancer Res 2006;12:465–72.
25. Hiraoka N, Onozato K, Kosuge T, Hirohashi S. Prevalence of FOXP3^{+} regulatory T cells increases during the progression of pancreatic ductal adenocarcinoma and its premalignant lesions. Clin Cancer Res 2006;12:5423–34.
26. Ormandy LA, Hillemann T, Wedemeyer H, Manns MP, Greten TF, Korangy F. Increased populations of regulatory T cells in peripheral blood of patients with hepatocellular carcinoma. Cancer Res 2005;65:2457–64.
27. Unitt E, Rushbrook SM, Marshall A, et al. Compromised lymphocytes infiltrate hepatocellular carcinoma: the role of T-regulatory cells. Hepatology 2005;41:722–30.
28. Yang XH, Yamagiwa S, Ichida T, et al. Increase of CD4^{+}CD25^{+} regulatory T-cells in the liver of patients with hepatocellular carcinoma. J Hepatol 2006;45:254–62.
29. Ruprecht CR, Gattorno M, Ferlito F, et al. Coexpression of CD25 and CD27 identifies Foxp3^{+} regulatory

T cells in inflamed synovia. J Exp Med 2005;201:1793–803.
30. Hirohashi S, Ishak KG, Kojiro M, et al. Hepatocellular carcinoma. In: Hamilton SR, Aaltonen LA, editors. Pathology and genetics of tumors of the digestive system. Lyon: IARC Press; 2000. p. 159–72.
31. Greene FL, Page DL, Fleming ID, et al. AJCC cancer staging manual. 6th ed. Chicago: Springer; 2002. p. 131–44.
32. Ishak K, Baptista A, Bianchi L, et al. Histological grading and staging of chronic hepatitis. J Hepatol 1995;22:696–9.
33. Takahashi Y, Akishima-fukasawa Y, Kobayashi N, et al. Prognostic value of tumor architecture, tumor-associated vascular characteristics, and expression of angiogenic molecules in pancreatic endocrine tumors. Clin Cancer Res 2007;13:187–96.
34. Okuda K, Nakanuma Y, Miyazaki M. Cholangiocarcinoma: recent progress. Part 1: Epidemiology and etiology. J Gastroenterol Hepatol 2002;17:1049–55.
35. Grabenbauer GG, Lahmer G, Distel L, Niedobitek G. Tumor-infiltrating cytotoxic T cells but not regulatory T cells predict outcome in anal squamous cell carcinoma. Clin Cancer Res 2006;12:3355–60.
36. Franco D, Capussotti L, Smadja C, et al. Resection of hepatocellular carcinomas: results in 72 European patients with cirrhosis. Gastroenterology 1990;98:733–8.
37. Izumi R, Shimizu K, Ii T, et al. Prognostic factors of hepatocellular carcinoma in patients undergoing hepatic resection. Gastroenterology 1994;106:720–7.
38. Oudejans JJ, Harijadi H, Kummer JA, et al. High numbers of granzyme B/CD8-positive tumor-infiltrating lymphocytes in nasopharyngeal carcinoma biopsies predict rapid fatal outcome in patients treated with curative intent. J Pathol 2002;198:468–75.
39. Ghiringhelli F, Menard C, Terme M, et al. CD4^{+}CD25^{+} regulatory T cells inhibit natural killer cell functions in a transforming growth factor-β-dependent manner. J Exp Med 2005;202:1075–85.
40. Tadokoro CE, Shakhar G, Shen S, et al. Regulatory T cells inhibit stable contacts between CD4^{+} T cells and dendritic cells in vivo. J Exp Med 2006;203:505–11.
41. Cabrera R, Tu Z, Xu R, et al. An immunomodulatory role for CD4^{+}CD25^{+} regulatory T lymphocytes in hepatitis C virus infection. Hepatology 2004;40:1062–73.
42. Stoop JN, van der Molen RG, Baan CC, et al. Regulatory T cells contribute to the impaired immune response in patients with chronic hepatitis B virus infection. Hepatology 2005;41:771–8.
43. Xu D, Fu J, Jin L, et al. Circulating and liver resident CD4^{+}CD25^{+} regulatory T cells actively influence the antiviral immune response and disease progression in patients with hepatitis B. J Immunol 2006;177:739–47.

Prognostic Value of Tumor Architecture, Tumor-Associated Vascular Characteristics, and Expression of Angiogenic Molecules in Pancreatic Endocrine Tumors

Yu Takahashi,[1,3] Yuri Akishima-Fukasawa,[1] Noritoshi Kobayashi,[1] Tsuyoshi Sano,[2] Tomoo Kosuge,[2] Yuji Nimura,[3] Yae Kanai,[1] and Nobuyoshi Hiraoka[1]

Abstract

Purpose: It is difficult to predict the biological behavior of pancreatic endocrine tumors (PETs). Our aim was to evaluate the prognostic significance of certain variables in PETs.

Experimental Design: The following variables were examined in 37 patients with PETs and then compared with other clinicopathologic characteristics: histologic tumor structure; microvessel density (MVD) measured by three different methods, including a unique method involving calculation of solid area MVD; endothelial proliferation; and the immunohistochemical expression of vascular endothelial growth factor-A and CXC chemokine CXCL-12. Intratumoral vascular structures were analyzed by double immunofluorescence using 30-μm-thick sections.

Results: The presence of focal and intensive solid growth of tumor cells (large solid nests; $P = 0.003$), low solid area MVD ($P = 0.002$), a high endothelial cell proliferation index (EPI; $P = 0.005$), and high expression of CXCL-12 in PET cells ($P = 0.018$) were significant unfavorable prognostic indicators. The predominant structure of the overall tumor histology and the expression of vascular endothelial growth factor-A did not separate aggressive PETs. In areas of focal solid growth, tumor-associated blood vessels had obviously low MVD and high EPI, and their structures were poorly formed with highly abnormal features, in comparison with other areas. High expression of CXCL-12 in tumor cells was significantly associated with variables representing tumor growth, hematogenous tumor spread, low MVD, high EPI, and the presence of large solid nests.

Conclusions: This study has provided novel findings on the prognostic features of tumor architecture and tumor-associated angiogenesis in PETs. CXCL-12 is the first candidate molecule in association with neoangiogenesis in PETs.

Pancreatic endocrine tumors (PETs) are uncommon neoplasms, and their prognostication is difficult when based purely on the histologic architecture and cytologic features of the tumor. Only the presence of distant metastases and local invasion to surrounding organs is the definitive criterion of malignancy (1–3). During the last few decades, various prognostic variables representing the proliferative or invasive

Authors' Affiliations: [1]Pathology Division, National Cancer Center Research Institute; [2]Division of Hepatobiliary and Pancreatic Surgery, National Cancer Center Hospital, Tokyo, Japan; and [3]Division of Surgical Oncology, Department of Surgery, Nagoya University Graduate School of Medicine, Nagoya, Japan

ability of tumor cells have been reported, such as tumor size, mitotic rate, Ki-67 proliferative index, and presence of vascular and perineural invasion (1–5). Other molecules have also been reported to be prognostic variables, such as cytokeratin 19 and CD99 (6, 7). The last WHO classification of PETs used some of these variables, in addition to conventional histopathologic tumor typing (1). However, this is still not enough for predicting the biological behavior of PETs because retrospective studies have shown that patients with PETs classified as "well-differentiated endocrine tumors," "benign tumors," or "tumors of uncertain behavior" sometimes suffer tumor recurrence or die of the disease (4, 6). To identify more reliable prognostic variables representing the biological characteristics of PETs, we analyzed their histologic structure, focusing especially on the solidness of the tumor growth pattern and attempted to classify them on this basis. At the same time, we examined the characteristics of intratumoral (i.t.) blood vessels, as these are closely associated with tumor architecture. In our experience, microvessel density (MVD) is lower in areas where tumor cells of PETs grow in a more solid pattern.

Normal endocrine tissues, including pancreatic islets of Langerhans and endocrine tumors, are characterized by high vascular density. In a murine pancreatic endocrine carcinoma model, RIP1-Tag2 transgenic mice expressing the SV40 T antigen in insulin-producing β cells, the tumor vasculature increases, and

vascular morphology become abnormal during multistep carcinogenesis (8, 9). Tumor-associated blood vessels in various human cancers are structurally and functionally abnormal, showing increased permeability, delayed maturation, and potential for rapid proliferation (10, 11). The vessel defects may also facilitate hematogenous spread of tumor cells (12). Angiogenesis is essential for tumor growth and also plays an important role in hematogenous spread (13, 14). Measurement of MVD using immunohistochemistry is a widely used method for measuring angiogenic activity. Numerous studies have shown that elevated MVD is a significant predictive indicator of poor survival (13, 15). In human PETs, however, some recent studies have shown that low MVD is an unfavorable prognostic factor (16, 17), whereas others have suggested that MVD is not a predictive indicator of survival (18, 19). Thus, the relationship between MVD and biological behavior in human PETs is still controversial, although high MVD does not seem to be an unfavorable prognostic factor. It has been shown that angiogenic factors in many kinds of human cancers are related to metastatic dissemination, tumor aggressiveness, and short patient survival (20–22). Only vascular endothelial growth factor-A (VEGF-A) has been studied in human PETs, although there is still no evidence that it contributes to malignancy or patient survival (16–18). No attempt has been made to assess the prognostic value of angiogenic factors other than VEGF-A in PETs.

The aim of the present study was to investigate histologic tumor architecture, tumor-associated angiogenesis, and expression of angiogenic molecules in a series of resected PETs and to evaluate the potential prognostic significance of these variables.

Materials and Methods

Patients and samples. This study was approved by the Ethics Committee of the National Cancer Center, Tokyo, Japan. Clinical and pathologic data and the specimens used for immunohistochemical analysis were obtained through a detailed retrospective review of the medical records of all 37 Japanese patients with PETs who had undergone initial surgical resection between 1981 and 2004 at the National Cancer Center Central Hospital, Japan. The median age of the patients at surgery was 55 years (range, 18-81 years; mean, 52.9 years). None of the patients had received prior therapy and underwent potentially curative resection: pancreatoduodenectomy in 19 cases, distal pancreatectomy in 12 cases, tumor enucleation in 4 cases, and total pancreatectomy in 2 cases. Tumors were classified according to the WHO classification (1) into the following groups: benign well-differentiated endocrine tumors (referred to as WHO-1 in this report), well-differentiated endocrine tumors of uncertain behavior (WHO-2), well-differentiated endocrine carcinoma (WHO-3), and poorly differentiated endocrine carcinoma (WHO-4). Follow-up was available in all cases and ranged from 2 to 275 months (median, 46.8 months; mean, 65.2 months). During the follow-up period, nine patients presented with evidence of disease progression as liver metastasis, and two of them presented with evidence of local recurrence. The latest survival data were collected on December 31, 2004. The total survival rate was 78% at 5 years and 65% at 10 years. The clinicopathologic features of the patients are summarized in Table 1. Eight variables (large tumor size, presence of invasion to surrounding organs, presence of lymph node metastasis, presence of hematogenous metastasis, presence of vascular invasion, presence of perineural invasion, absence of functional hormone syndrome, and high Ki-67 index) had been reported to be unfavorable prognostic factors (1, 2). In our series, all these variables except "absence of functional hormone syndrome" were closely correlated with short survival (Table S1).

For histopathologic examinations, all tissue specimen was cut to make sections. Four-micrometer formalin-fixed, paraffin-embedded sections were prepared and stained with H&E. Vascular invasion was assessed by histopathologic examination, using H&E-stained tissue sections and sections stained for elastic fibers with Maeda's resorcin/fuchsin solution (Muto Pure Chemicals, Tokyo, Japan). With regard to the structural pattern of tumor histology, tumors were divided into four groups by the following criteria based on predominant architecture (Fig. 1A-D): grade 1, tumors consisting of small nests (with 1-5 tumor cells in the minor axis); grade 2, tumors consisting of moderate nests (with 6-10 tumor cells in the minor axis); grade 3, tumors consisting of large solid nests (with ≥11 tumor cells in the minor axis); and grade 4, tumors showing a diffuse growth pattern. The ratio of each solid grade was determined each tumor area in middle-power view and was calculated for the entire tumor area. Then the predominant grades were determined for each PET. PET with large solid nests was defined if there was at least a large solid nest in the tumor, regardless of the overall solid grading. Grading was carried out by two observers independently.

Immunohistochemistry. Immunohistochemistry was done on the formalin-fixed, paraffin-embedded tissue sections using the avidin-biotin complex method as described previously (23). We used 4-μm-thick sections of representative blocks with antibodies against the

Table 1. Summary of patients' demographics

Variables	WHO-1 (*n* = 6)	WHO-2 (*n* = 14)	WHO-3 (*n* = 15)	WHO-4 (*n* = 2)	Total
Sex (male/female)	2/4	6/8	6/9	1/1	15/22
Median age (y)	58.5	55.5	52	30	55
Functional hormone syndrome*	0	2	2	0	4
Mean tumor size (cm)	1.2	3.6	6.4	10.0	4.7
Invasion to surrounding organs	0	0	10	2	12
Lymph node metastasis	0	0	13	2	15
Hematogenous metastasis†	0	1	8	1	10
Vascular invasion	0	4	13	2	19
Perineural invasion	0	3	10	2	15
Ki-67 labeling index >5	0	4	10	2	16
Follow-up					
Alive and well without disease	5	13	7	1	26
Alive with disease	0	0	3	0	3
Dead of disease	0	1	4	1	6
Dead of other cause	1	0	1	0	2

*Four patients showed the clinical manifestation associated with hypersecretion of insulin in two cases: glucagon in one and gastrin in another.
†Tumor metastasized to liver or other organs by hematogenous spreading before and/or after the surgical resection of PETs.

following: chromogranin A (poly; 1:500), synaptophysin (poly; 1:50), neuron-specific enolase (BBS/NC/VI-H14; 1:100), CD31 (JC/70A; 1:50), CD34 (QBEnd 10; 1:100), Factor VIII (poly; 1:1000), α-smooth muscle actin (α-SMA; 1A4; 1:50), and Ki-67 (MIB-1; 1:100) from DAKO (Glostrup, Denmark); CD56 (NCC-Lu-243; 1:50) from Nippon Kayaku (Tokyo, Japan); VEGF-A (poly; 1:100) from Santa Cruz Biotechnology (Santa Cruz, CA); and CXCL-12 (79018; 1:50) from R&D Systems, Inc. (Minneapolis, MN). As a brief description, the sections were deparaffinized and rehydrated. After blocking of endogenous peroxidase with methanol containing 0.3% H_2O_2, the sections were autoclaved at 121°C for 10 min in citrate buffer (10 mmol/L sodium citrate, pH 6) for antigen retrieval. After blocking with normal goat serum, the sections were reacted overnight with appropriately diluted primary antibodies. The sections were then reacted sequentially with biotin-conjugated anti-mouse immunoglobulin G antibodies (Vector Laboratories, Burlingame, CA) and Vectastain Elite ABC reagent (Vector Laboratories). For staining VEGF-A, the sections were boiled at 95°C for 10 min for antigen retrieval. Diaminobenzidine was used as the chromogen, and the nuclei were counterstained with hematoxylin. For semiquantitative assessments of the immunohistochemical results for VEGF-A and CXCL-12, cytoplasmic staining intensity and the proportion of positive tumor cells were recorded. A staining index (with a value of 0-9) was calculated as the product of staining intensity (0-3) and area of positive staining (0, <1%; 1, 1-10%; 2, 10-50%; 3, >50%; ref. 23). The upper quartile was used as the cutoff point. The Ki-67 labeling index was determined as described previously (23). Immunohistochemical double staining for CD34 and Ki-67 was also done as described previously (24). Initially, Ki-67 was stained and visualized with diaminobenzidine as a brown-colored chromogen, followed by detachment of antibodies; then secondary immunohistochemistry was done to detect CD34; and the reaction product was visualized with VIP as a purple-colored chromogen (Vector Laboratories).

Evaluation of i.t. MVD. For evaluation of i.t. MVD, microvessels were detected by morphologic observation and immunohistochemical labeling with the endothelial markers CD31, CD34, and Factor VIII. In our preliminary study, three different markers detected endothelial cells similarly. CD34 showed the strongest intensity among them and could detect endothelial cells easily, but sometimes, it labeled fibroblasts that could be easily distinguished from vascular endothelial cells by their histology. Factor VIII showed the weakest staining intensity among them. Then we used CD34 for MVD assay and CD31 for immunofluorescence double staining. All independent CD34-positive vessel structures were counted, irrespective of the presence of an identifiable lumen. For assessment of MVD, we used three different methods as follows. Average MVD (Av-MVD) was analyzed by selecting 10 randomized fields per tumor at a magnification of ×200 (0.95 mm² per field), and the number of CD34-positive vessel structures in each field was counted. The mean number of vessels was then calculated after exclusion of the lowest and highest values measured (16). Hotspot MVD was assessed by a modification of the Weidner technique (21). The H&E-stained tissue sections were screened, and three areas with the most intense vascularization were selected at low magnification. We then counted CD34-positive vessels at a magnification of ×200, and the average counts for the three fields were calculated. For solid area MVD (S-MVD), the H&E-stained tissue sections were screened, and we selected three areas showing the most solid growth pattern of tumor cells, which often contained large solid nests or a diffuse growth pattern. Then CD34-positive vessels at a magnification of ×200 were counted in each corresponding area. The average counts of the three fields was calculated and defined as the S-MVD. Two observers, having no access to the patient data, evaluated independently MVD, morphometrical vessel characters, and proliferating endothelial cells described below. Their final value was the average of the value counted by the two observers. To assess intraobserver reproducibility, several tissue sections were counted thrice by each observer. To assess interobserver reproducibility, 10 data counted by each observer for the same tumor were compared (16).

Immunofluorescence double staining. Immunofluorescence double staining was done on 30-μm-thick, formalin-fixed, paraffin-embedded tissue sections as described previously (24), with some modifications. All antibodies were diluted in 0.2% Triton X-100 and 5% skim milk in TBS-T. α-SMA antigens were stained by the CSA system (DAKO) with our modification, and then CD31 was stained with CSAII (DAKO). Reaction time for the primary and secondary antibodies was extended to overnight and 1 h, respectively. After reaction with biotin-conjugated tyramide solution, the sections were incubated with Texas Red–conjugated avidin (1:200) for 1 h at room temperature. After detaching the antibodies by acid treatment (100 mmol/L glycine/HCl, pH 2.2) for 2 h, the sections were stained with CD31 using CSAII according to the manufacturer's instructions with modifications. Just after reaction of the sections with FITC-conjugated tyramide, the sections were washed and mounted with Vectashield mounting medium (Vector Laboratories). Immunostained tissue sections were analyzed with a confocal microscope (LSM5 Pascal; Carl Zeiss Jena GmbH, Jena, Germany) equipped with a 15-mW Kr/Ar laser. The confocal files were saved, compiled, and fused to make three-dimensional pictures.

To estimate the branching frequency of blood vessels, 12 randomized fields were selected for each tumor at a magnification of ×200. The distance of blood vessels between the closest two branches in each field was measured, and the mean length for each tumor was calculated, which we termed the unbranched vessel length. To estimate variability in the luminal diameter of blood vessels, 12 randomized fields were selected for each tumor at a magnification of ×400. The maximum and minimum luminal diameters of blood vessels between the closest two branches in each field were measured, and the average of the difference in diameter was calculated. To evaluate abnormality of blood vessels showing irregular vessel wall shapes and distortion, i.t. vessels were divided into five categories: category 1 corresponded to regular vessels in normal islets of Langerhans, category 5 corresponded to the most severely changed vessels as shown in Fig. 4G to I, and categories 2 to 4 corresponded to vessels with mild to severe abnormalities between categories 1 and 5.

Endothelial cell proliferation in i.t. blood vessels. To evaluate the proliferation of endothelial cells, tumor tissues that had been double stained for Ki-67 and CD34 were assessed by modified previous methods (25, 26). Fifty randomized fields at a high magnification (×400) were selected for each tumor, and we counted the number of CD34-expressing endothelial cells with Ki-67–positive nuclei in each field, then the total amount was defined as the endothelial cell proliferation (ECP). The ECP proliferation index (EPI) was defined as the ECP divided by the Av-MVD that was assessed in the same fields because MVD was different in each tumor.

Statistical analysis. Statistical analyses were done with StatView-J 5.0 software (Abacus Concepts, Berkeley, CA) and SPSS statistical software version 12.0 (SPSS, Inc., Chicago, IL). Association between categorical variables was examined by Fisher's exact probability test. Mann-Whitney nonparametric tests were used to compare categorical with continuous tumor variables when there were two categories, whereas Kruskal-Wallis nonparametric tests were used instead when there were more than two categories. Differences at $P < 0.05$ were considered significant. Survival rates were computed by the Kaplan-Meier method and compared by the log-rank test.

Results

The clinicopathologic characteristics of the 37 patients with PETs are described in Materials and Methods and Table 1.

Histologic structural pattern. The histologic pattern of tumor growth was studied to clarify whether it could predict tumor behavior. Initially, we classified PETs into four categories based on the solidness of the predominant tumor histology, ranging from grade 1, which was least solid, to grade 4, which showed
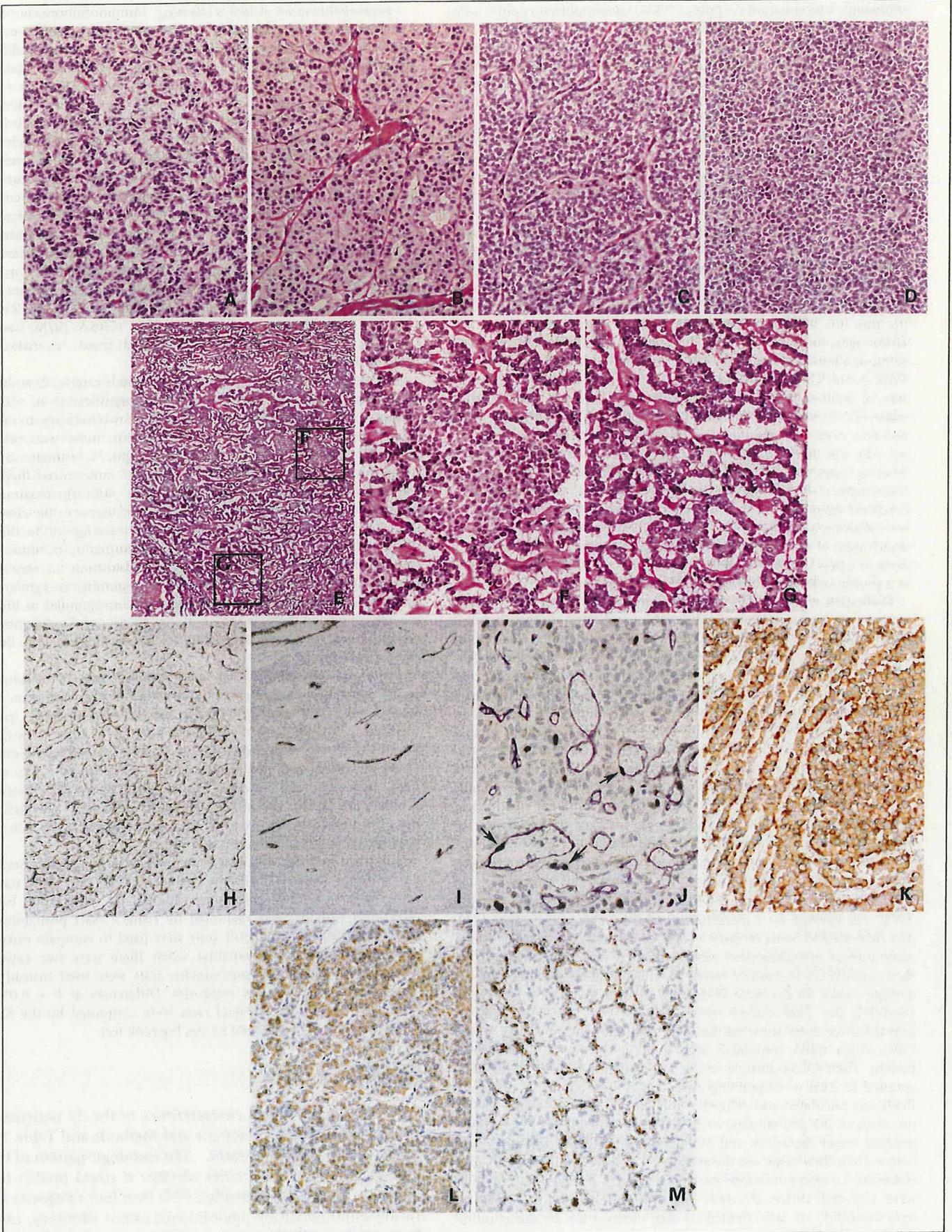
the most solid and diffuse growth (Fig. 1A-D). Most of the PETs were classified as grade 1 (19 of 37; Table 2), which included tumors with a predominant histologic structure showing a thin trabecular, gyriform, or pseudoglandular pattern. All of the grade 3 PETs belonged to WHO-3, and grade 4 PETs belonged to WHO-4. There was no significant correlation between any of the grades and disease-free survival, but disease-free survival became closely correlated when grade 1 and 2 PETs were combined (Fig. 2A).

We then selected PETs that had a "large solid nest" defined as the presence of ≥ 11 tumor cells in the minor axis, independent of the overall tumor histologic pattern (Fig. 1E-G). Twenty PETs had large solid nests, including five grade 1 PETs, seven grade 2 PETs, and eight grade 3 and grade 4 PETs (Table 2). Interestingly, all the patients that suffered tumor recurrence had PETs with large solid nests, and all the patients without large solid nests remained disease-free. The presence of large solid nests was a significant factor correlated with disease-free survival (log-rank test, $P = 0.003$; Fig. 2B). The presence of large solid nests was significantly correlated with tumor size ($P = 0.008$), invasion to surrounding organs ($P = 0.002$), lymph node metastasis ($P = 0.018$), hematogenous metastasis ($P = 0.0006$), vascular invasion ($P = 0.0002$), and Ki-67 index ($P = 0.007$; Table S1).

MVD. The relationship between MVD and biological behavior in human PETs is controversial (16–18), probably as a result of how MVD is counted. To clarify whether MVD is related to tumor behavior and to select the best way to count MVD, we tried to measure MVD of PETs using three different counting methods (Materials and Methods; Fig. 1H and I): Av-MVD, hotspot MVD, and S-MVD. Av-MVD ranged from 59.4 to 423.5 vessels per field (mean, 189.1; median, 167.6); hotspot MVD ranged from 132.3 to 625.0 vessels per field (mean, 288.3; median, 268.0); and S-MVD ranged from 30.0 to 468.3 vessels per field (mean, 161.5; median, 132.3). Av-MVD and S-MVD decreased according to the progression of PETs by the WHO classification, and this was statistically significant (Kruskal-Wallis test: Av-MVD, $P = 0.010$; S-MVD, $P = 0.003$; Fig. 3A and Fig. S1). Hotspot MVD did not show apparent differences among the WHO classes ($P = 0.500$; Fig. S1). When all the PETs were divided into two groups based on median MVD, the high MVD group showed longer patient survival than the low MVD group (Fig. 3B and Fig. S1). The difference was clearer for S-MVD (log-rank test, $P = 0.002$), and the high S-MVD group included no patients with recurrent tumors. S-MVD was significantly correlated with tumor size ($P = 0.002$), invasion to surrounding organs ($P = 0.001$), lymph node metastasis ($P = 0.0006$), hematogenous metastasis ($P = 0.0004$), vascular invasion ($P < 0.0001$), perineural invasion ($P = 0.007$), and Ki-67 index ($P = 0.0002$; Table S1).

Vascular ECP. The dynamics of neoangiogenesis in PETs was assessed by ECP (Materials and Methods; Fig. 1J). ECP ranged from 0 to 26 (mean, 7.59; median, 7). Surprisingly, the ECP was higher in low S-MVD tumors ($P = 0.011$; Fig. 3C). EPI (Materials and Methods; range, 0.00-0.27; mean, 0.057;

Table 2. Relationship between histologic structural grades or tumors with large solid nests and WHO classification of pancreatic endocrine tumors

	Grade 1	Grade 2	Grade 3	Grade 4	Total cases
WHO-1	4 (1)	2 (2)	0	0	6 (3)
WHO-2	11 (2)*	3 (1)	0	0	14 (3)
WHO-3	4 (2)**	5 (4)*	6 (6)****	0	15 (12)
WHO-4	0	0	0	2 (2)*	2 (2)
Total	19 (5)	10 (7)	6 (6)	2 (2)	37 (20)

NOTE: The numbers of patients with PET having large solid nests are in parentheses.
*n, number of asterisks (*) represent numbers of patients with PET recurrence.

median, 0.038) was also higher in PETs with low S-MVD and was significantly correlated with WHO classification (Kruskal-Wallis test, $P = 0.001$; Fig. 3D). When patients were divided into two groups by the median EPI, the high EPI group showed significantly shorter disease-free survival than the low EPI group (log-rank test, $P = 0.005$; Fig. 3E). EPI was significantly correlated with tumor size ($P < 0.0001$), invasion to surrounding organs ($P = 0.005$), lymph node metastasis ($P = 0.020$), hematogenous metastasis ($P = 0.003$), vascular invasion ($P < 0.0001$), and Ki-67 index ($P = 0.0008$; Table S1).

Vascular characteristics. We then analyzed the structures of blood vessels to determine whether blood vessels change to poorly formed vessels with multiple abnormalities, in association with tumor progression. We analyzed 9 PETs with high S-MVD and 13 PETs with low S-MVD that were available for immunofluorescence analysis using 30-μm-thick tissue sections stained for CD31 and α-SMA. There were fine mesh-like structures consisting of smooth, thin, and relatively regular vessels in tumors with high S-MVD (Figs. 1H and 4D-F). The rough structure of the vasculature in tumors with high S-MVD was similar to the vascular features of normal islets of Langerhans (Fig. 4A-C), although the vessels in the tumors were thick, and their detailed structures were irregular. In contrast, the vasculature in PETs with low S-MVD was less branched and relatively straight (Fig. 4J), consisting of thicker, more irregularly shaped and often distorted vessels (Figs. 1I, 4G-I and 4L). In high-power view, instead of mature branches, there were many very small and irregular buds on the vessels, which showed highly abnormal features (Fig. 4I). α-SMA–positive cells covered these irregular buds. The luminal diameter of vessels was more variable in PETs with low S-MVD than in PETs with high S-MVD (Fig. 4K). Almost all the i.t. blood vessels were covered by α-SMA–positive mural cells, although α-SMA–positive multiple layers were often observed in PETs with low S-MVD. These findings indicated that i.t. blood vessels in PETs with low S-MVD were poorly formed blood vessels with multiple abnormalities,

Fig. 1. *A* to *D*, histologic structural grading of PETs based on the degree of solid growth of tumor cells in the predominant architecture. Grade 1 tumor consists of small nests (*A*). Grade 2 tumor consists of moderate nests (*B*). Grade 3 tumor consists of large solid nests (*C*). Grade 4 tumor grows in a diffuse solid pattern (*D*). *E* to *G*, large solid nests. Tumor cells proliferate predominantly in a trabecular pattern and sometimes form large solid nests focally in low-power view (*E*). Middle-power view of large solid nests (*F*) and trabecular pattern (*G*). *H* to *M*, immunohistochemistry. CD34-labeled endothelial cells are detected in PET with high MVD (*H*) and in PET with low MVD (*I*) in low-power view. *J*, CD34 (*purple*) is expressed in vascular endothelial cells, and nuclei of proliferating cells are labeled by Ki-67 (*brown*) in high-power view. Arrows, proliferating endothelial cells. *K*, VEGF-A stained in cytoplasm of PET cells in middle-power view. CXCL-12 stained in PET cells (*L*) and blood vessels (*M*) in middle-power view.
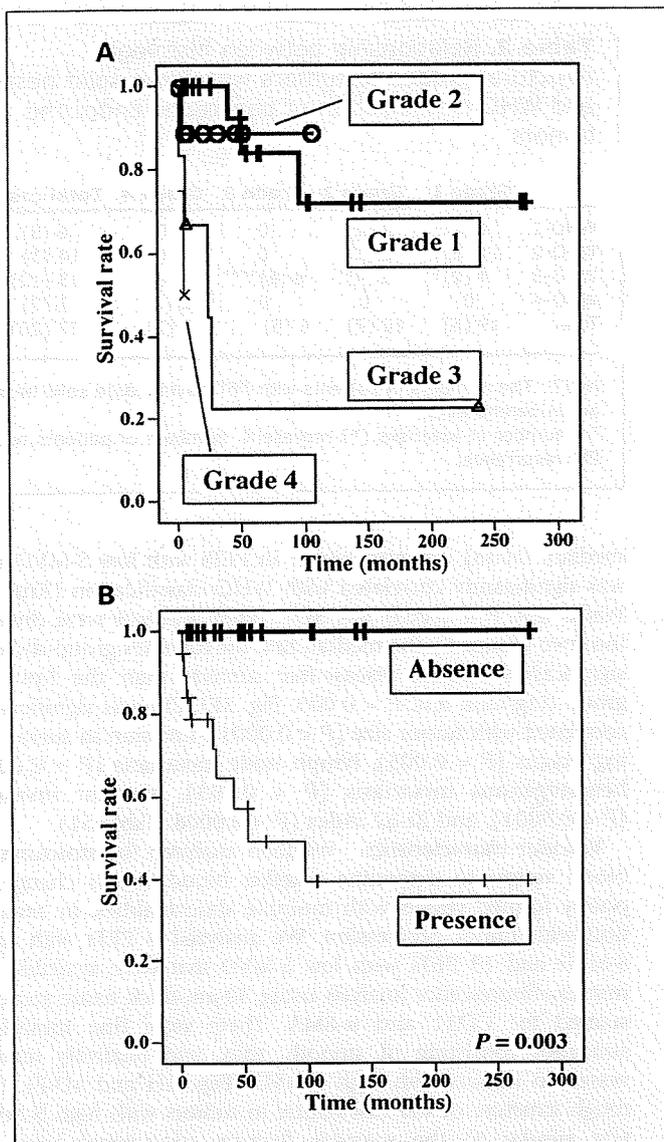
Fig. 2. Kaplan-Meier survival curves of the 37 patients with PETs. *A,* PETs are classified by predominant histological structures into four grades. There was no significant correlation between this classification and disease-free survival. *B,* PETs are divided by the presence or absence of large solid nests. Patients with PETs showing large solid nests had significantly shorter disease-free survival (log-rank test, *P* = 0.003).

whereas blood vessels in PETs with high S-MVD still had the characteristics of endocrine organs.

Expression of VEGF-A and CXCL-12 in PETs. To assess the angiogenic factors in PETs, we analyzed the expression of VEGF-A and CXCL-12 in tumor cells and i.t. blood vessels by immunohistochemistry (Fig. 1K-M). CXCL-12 is known to be a CXC chemokine involved in the recruitment of circulating endothelial progenitor cells from bone marrow to the target organs (27, 28). High expression of CXCL-12 in tumor cells was significantly correlated with high EPI (*P* = 0.020; Table 3) and low S-MVD (*P* = 0.0006; Table 3), although expression of CXCL-12 in i.t. blood vessels and VEGF-A expressed in tumor cells did not closely correlate with EPI and S-MVD (Table 3). High expression of VEGF-A in tumor cells was significantly correlated with high expression of CXCL-12 in i.t. blood vessels

(*P* < 0.0001) but not to other clinicopathologic variables, including expression of CXCL-12 in tumor cells (Table 3). A high value of CXCL-12 in the tumor was significantly correlated with marked vascular invasion (*P* = 0.0006), the presence of hematogenous metastasis (*P* = 0.006), large tumor size (*P* = 0.035), a high Ki-67 index (*P* = 0.006), and the presence of large solid nests (*P* = 0.018). Furthermore, PETs having high amounts of CXCL-12 in the tumor cells were closely correlated with a shorter disease-free patient survival rate (log-rank test, *P* = 0.018; Fig. 3F).

Discussion

In this study, we found a new histologic marker for predicting the biological behavior of PETs (i.e., "the presence of focal large solid nests"), which is independent of the predominant histologic structure. Then we measured S-MVD and showed a close correlation between low MVD and an unfavorable prognosis in PETs. Paradoxically, i.t. vessels of PETs with a high MVD showed low EPI and vice versa. Morphometric analysis showed that blood vessels in PETs with low MVD were more poorly formed and had more irregular and abnormal features, whereas blood vessels in PETs with high MVD showed relatively regular mesh-like features similar to vessels in normal islets of Langerhans. These findings imply that a high MVD seems to be a characteristic of blood vessels in islets of Langerhans, and that EPI can be a hallmark of angiogenic activity in tumor-associated blood vessels in PETs. Our data also suggest that EPI and S-MVD are predictors of the biological behavior of PETs. We analyzed angiogenic factors in PETs and found that high EPI and low MVD were significantly correlated with high expression of CXCL-12 in tumor cells but not with the expression of CXCL-12 in i.t. blood vessels and VEGF-A. Combined with the data for the relationship between CXCL-12 and other variables, it is suggested that CXCL-12 produced in tumor cells is involved in the angiogenesis of tumor-associated vessels and hematogenous spread as well as proliferation of tumor cells and thus may contribute to the aggressiveness of PETs. CXCL-12 is the first molecule to be highlighted as a possible angiogenic factor playing important roles in the neoangiogenesis of PETs. Thus, we have provided novel data on the prognostic features of tumor architecture and tumor-associated angiogenesis in PETs.

In contrast to the predominant histologic structures, the presence of focal large solid nests delineated PETs with aggressive behavior. Even in grade 1 and 2 PETs, patients with large solid nests had significantly shorter disease-free survival than patients without them (*P* = 0.024). Interestingly, metastatic PETs showed almost the same histologic architecture as the original pancreatic tumors and were not occupied by tumor cells with solid growth. These findings suggest that tumor cells in large solid nests are not more progressed or more malignant than their origin, and that the presence of large solid nests represents the potential for tumor malignancy.

By comparing three methods for evaluation of MVD, we found that the best variable for predicting the representative biological characteristics of PETs was S-MVD. This seems reasonable because in PETs, we showed that a focal tumor structure showing the most solid growth represents the behavior of the tumor as a whole. Morphometric analysis also showed that irregularity and abnormality of i.t. blood vessels were associated with tumor growth pattern where the vessels were present. These findings

imply that tumor architecture is closely correlated with local vessel formation, and that tumor cells and blood vessels seem to be a pair of components within a single structure.

Our results indicate that EPI and MVD can be prognostic variables in patients with PETs. Abnormal tumor-associated blood vessels tend to grow rapidly (10), consistent with the fact that PETs with more poorly formed blood vessels have a high

EPI. EPI is also significantly correlated with hematogenous spread (vascular invasion, $P < 0.0001$; hematogenous metastasis, $P = 0.003$) and survival ($P = 0.005$) in PETs. Recently, similar results were indicated in the other tumor by Stefansson et al. That is, increased vascular proliferation was associated with aggressive features of tumors and was an independent prognostic factor in endometrial carcinoma (26).

Fig. 3. *A, C,* and *D,* relationship between vascular index and WHO classification. *B, E,* and *F,* Kaplan-Meier survival curves of 37 patients with PETs. *A,* S-MVD significantly decreased according to progression of PETs in terms of the WHO classification (Kruskal-Wallis test, $P = 0.003$). *B,* patients were divided into two groups by median S-MVD. The high S-MVD group showed significantly longer survival than the low S-MVD group (log-rank test, $P = 0.002$). *C,* EPC significantly increased according to progression of PETs in terms of the WHO classification (Kruskal-Wallis test, $P = 0.019$). *D,* EPI significantly increased according to progression of PETs in terms of the WHO classification (Kruskal-Wallis test, $P = 0.001$). *E,* patients were divided into two groups by median EPI. The high EPI group showed significantly shorter survival than the low EPI group (log-rank test, $P = 0.005$). *F,* patients were divided into two groups by the quartile value of CXCL-12 expressed in the tumor cells. Patients with PETs showing high expression of CXCL-12 in the tumor cells had significantly shorter survival than those whose tumors showed low expression (log-rank test, $P = 0.018$).
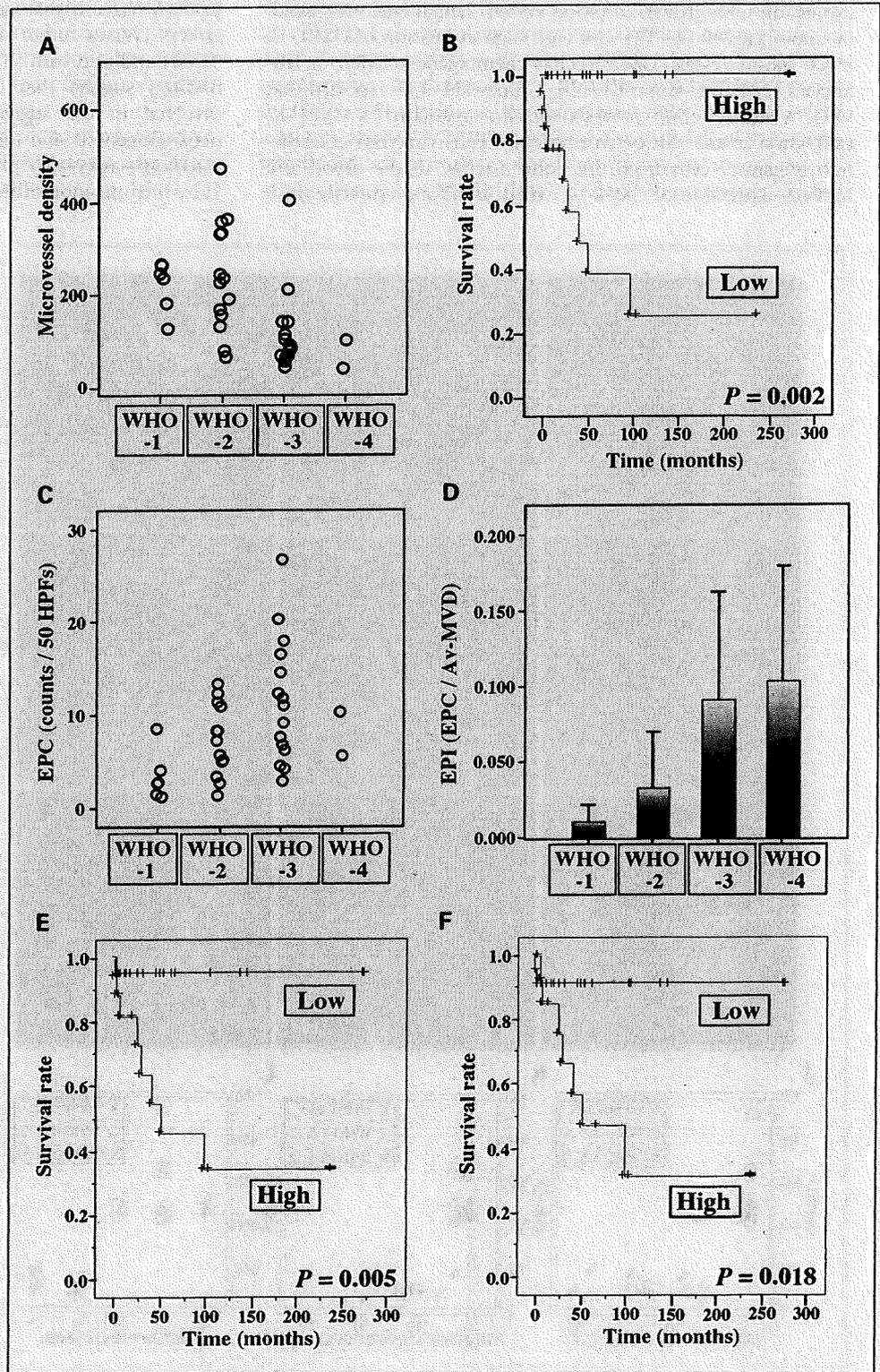
What kinds of molecules are involved in tumor-associated angiogenesis in PETs? It has been reported that in many kinds of cancers VEGF produced in tumor cells accelerates tumor-associated angiogenesis, leading to tumor growth and a high frequency of hematogenous tumor cell spread (14). VEGF-A expression in PETs is reported to be not closely correlated with MVD (16, 18) or to be closely correlated with high MVD (17). In our series, there was no close correlation of VEGF-A expression with growth of blood vessels, hematogenous spread, or tumor growth in PETs, but with high expression of CXCL-12 in i.t. blood vessels. CXCL-12 has chemotactic activity for leukocytes (28) and stem cells (29). Grunewald et al. reported that VEGF-A induces adult neovascularization mediated by CXCL-12 expression in the microenvironment. VEGF-A recruits endothelial progenitor cells from the bone marrow to the blood and induces expression of CXCL-12, which traps and correctly positions endothelial progenitor cells around growing vessels in tissues (27). Our study suggested that VEGF-A induced the expression of CXCL-12 in tumor vessels, although such events did not lead to tumor-associated neoangiogenesis in PETs. In contrast, high EPI was closely correlated with high CXCL-12 produced in tumor cells ($P = 0.020$). High expression of CXCL-12 in tumor cells was also positively correlated with variables of hematogenous tumor spread (versus vascular invasion, $P = 0.0006$; versus hematogenous metastasis, $P = 0.006$) and tumor growth (versus tumor size, $P = 0.035$; versus Ki-67 index, $P = 0.006$) and also with shorter patient survival ($P = 0.018$). These findings suggest that CXCL-12 produced in tumor cells is involved in the aggressive features of tumor mediated by neoangiogenesis and tumor growth. Orimo et al. reported that carcinoma-associated fibroblasts in breast cancer secrete CXCL-12, which promotes the growth of the tumor cells both directly
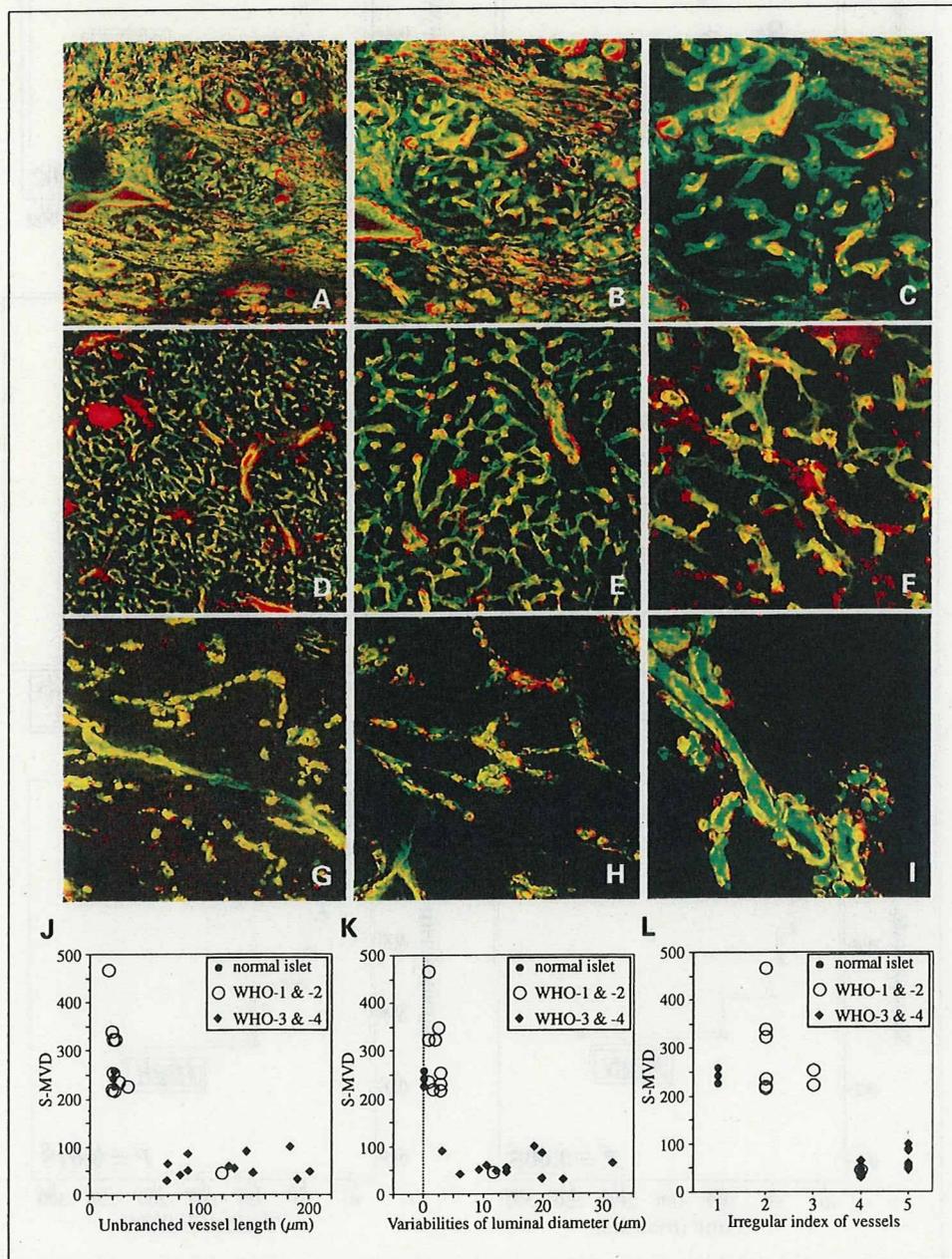
Fig. 4. Characterization of tumor-associated blood vessels in double immunofluorescence examination of CD31 (*green*) and α-SMA (*red*) using 30-μm-thick sections. Normal islet of Langerhans in low-power (*A*), middle-power (*B*), and high-power (*C*) view. PET with high S-MVD in low-power (*D*), middle-power (*E*), and high-power (*F*) view. PET with low S-MVD in low-power (*G*), middle-power (*H*), and high-power (*I*) view. *J* to *L*, morphometric analyses of PETs. I.t. blood vessels were examined for unbranched vessel length (*J*), variability of luminal diameter (*K*), and vessel irregularity (*L*).

Table 3. Relationship between clinicopathologic variables and VEGF-A or CXCL-12

Variables	n	VEGF-A			CXCL-12 in tumor cells			CXCL-12 in blood vessels		
		High (n = 19)	Low (n = 18)	P	High (n = 19)	Low (n = 18)	P	High (n = 19)	Low (n = 18)	P
Age (y)										
≤55	19	8	11	NS	8	11	NS	8	11	NS
>55	18	10	8		7	11		11	7	
Sex										
Female	22	13	9	NS	10	12	NS	13	9	NS
Male	15	5	10		5	10		6	9	
Functional hormone syndrome										
Absence	33	16	17	NS	14	19	NS	17	16	NS
Presence	4	2	2		1	3		2	2	
Tumor size (cm)										
<2	13	3	10	0.038	2	11	0.035	4	9	NS
≥2	24	15	9		13	11		15	9	
Invasion to surrounding organs										
Absence	25	12	13	NS	7	18	NS	15	10	NS
Presence	12	6	6		8	4		4	8	
Lymph node metastasis										
Absence	22	8	14	NS	6	16	NS	11	11	NS
Presence	15	10	5		9	6		8	7	
Hematogenous metastasis*										
Absence	27	12	15	NS	7	20	0.006	13	14	NS
Presence	10	6	4		8	2		6	4	
Vascular invasion										
Absence	18	6	12	NS	2	16	0.0006	9	9	NS
Presence	19	12	7		13	6		10	9	
Perineural invasion										
Absence	22	10	12	NS	7	15	NS	12	10	NS
Presence	15	8	7		8	7		7	8	
Ki-67 labeling index										
≤5	21	8	13	NS	4	17	0.006	9	12	NS
>5	16	10	6		11	5		10	6	
Histologic structural grades										
1 + 2	29	15	14	NS	10	19	NS	18	11	0.019
3 + 4	8	3	5		5	3		1	7	
Large solid nests										
Absence	17	7	10	NS	3	14	0.018	9	8	NS
Presence	20	11	9		12	8		10	10	
S-MVD										
High	18	7	11	NS	2	16	0.0006	10	8	NS
Low	19	11	8		13	6		9	10	
EPI										
High	18	11	7	NS	11	7	0.020	10	8	NS
Low	19	7	12		4	15		9	10	
VEGF-A										
High	18				10	8	NS	16	2	<0.0001
Low	19				5	14		3	16	
CXCL-12 in tumor cells										
High	15	10	5	NS				8	7	NS
Low	22	8	14					11	11	
CXCL-12 in vessels										
High	19	16	3	<0.0001	8	11	NS			
Low	18	2	16		7	11				

Abbreviation: NS, not significant.
*Tumor metastasized to liver or other organs by hematogenous spreading before and/or after the surgical resection of PETs.

and indirectly, and promotes neoangiogenesis by recruiting endothelial progenitor cells (30). Finally, high expression of CXCL-12 in tumor cells had a close correlation with the presence of large solid nests ($P = 0.018$). It is possible that CXCL-12 produced by tumor cells may mediate the formation of focal solid structures by a pair of solid growing tumor cells and their surrounding tumor-associated blood vessels with highly abnormal features. Furthermore, it is suggested that interrupting the angiogenic pathway mediated by CXCL-12 may provide a novel and efficient antiangiogenesis strategy for the treatment of PETs.

Acknowledgments

References

1. DeLellis RA, Lloyd RV, Heitz PU, Eng C. World Health Organization classification of tumours. Pathology and genetics of tumours of endocrine organs. Lyon: IARC Press; 2004. p. 175–208.

2. Solcia E, Capella C, Klöppel G. Tumors of the pancreas. Atlas of tumor pathology. 3rd series, fascicle 20. Washington (DC): Armed Forces Institute of Pathology; 1997.

3. Maderia I, Terris B, Voss M, et al. Prognostic factors in patients with endocrine tumours of the duodenopancreatic area. Gut 1998;43:422–7.

4. Hochwald SN, Zee S, Conlon KC, et al. Prognostic factors in pancreatic endocrine neoplasms: an analysis of 136 cases with a proposal for low-grade and intermediate-grade groups. J Clin Oncol 2002;20: 2633–42.

5. Jorda M, Ghorab Z, Fernandez G, Nassiri M, Hanly A, Nadji M. Low nuclear proliferative activity is associated with nonmetastatic islet cell tumors. Arch Pathol Lab Med 2003;127:196–9.

6. Deshpande V, Castillo CF, Muzikansky A, et al. Cytokeratin 19 is a powerful predictor of survival in pancreatic endocrine tumors. Am J Surg Pathol 2004;28: 1145–53.

7. Goto A, Niki T, Terada Y, Fukushima J, Fukayama M. Prevalence of CD99 protein expression in pancreatic endocrine tumors (PETs). Histopathology 2004;45: 384–92.

8. Hanahan D, Folkman J. Patterns and emerging mechanisms of the angiogenic switch during tumorigenesis. Cell 1996;86:353–64.

9. Lopez T, Hanahan D. Elevated levels of IGF-1 receptor convey invasive and metastatic capability in a mouse model of pancreatic islet tumorigenesis. Cancer Cell 2002;1:339–53.

10. Jain RK. Molecular regulation of vessel maturation. Nat Med 2003;9:685–93.

11. Morikawa S, Baluk P, Kaidoh T, et al. Abnormalities in pericytes on blood vessels and endothelial sprouts in tumors. Am J Pathol 2002;160:985–1000.

12. Hashizume H, Baluk P, Morikawa S, et al. Openings between defective endothelial cells explain tumor vessel leakiness. Am J Pathol 2000;156:1363–80.

13. Ellis LM, Fidler IJ. Tumor angiogenesis. In: Mendelsohn J, Howley PM, Israel MA, et al. editors. The molecular basis of cancer. 2nd ed. Philadelphia: Saunders; 2001. p. 173–85.

14. Carmeliet P, Jain RK. Angiogenesis in cancer and other diseases. Nature 2000;407:249–57.

15. Poon RTP, Ng IOL, Lau C, et al. Tumor microvessel density as a predictor of recurrence after resection of hepatocellular carcinoma: a prospective study. J Clin Oncol 2002;20:1775–85.

16. Marion-Audibert AM, Barel C, Gouysse G, et al. Low microvessel density is an unfavorable histoprognostic factor in pancreatic endocrine tumors. Gastroenterology 2003;125:1094–104.

17. Couvelard A, O'Toole D, Turley H, et al. Microvascular density and hypoxia-inducible factor pathway in pancreatic endocrine tumours: negative correlation of microvascular density and VEGF expression with tumour progression. Br J Cancer 2005;92:94–101.

18. La Rosa S, Uccella S, Finzi G, Alvarello L, Sessa F, Capella C. Localization of vascular endothelial growth factor and its receptors in digestive endocrine tumors: correlation with microvessel density and clinicopathologic features. Hum Pathol 2003;34:18–27.

19. Tan G, Cioc AM, Perez-Montiel D, Ellison EC, Frankel WL. Microvascular density does not correlate with histopathology and outcome in neuroendocrine tumors of the pancreas. Appl Immunohistochem Mol Morphol 2004;12:31–5.

20. Folkman J. Clinical applications of research on angiogenesis. N Engl J Med 1995;333:1757–63.

21. Weidner N. Tumoural vascularity as a prognostic factor in cancer patients: the evidence continues to grow. J Pathol 1998;184:119–22.

22. Weidner N, Semple JP, Welch WR, Folkman J. Tumor angiogenesis and metastasis - correlation in invasive breast carcinoma. N Engl J Med 1991;324:1–8.

23. Takahashi Y, Hiraoka N, Onozato K, et al. Solid-pseudopapillary neoplasms of the pancreas in men and women: do they differ? Virchows Arch 2006;448: 561–9.

24. Hiraoka N, Onozato K, Kosuge T, Hirohashi S. Prevalence of FOXP3$^+$ regulatory T cells increases during the progression of pancreatic ductal adenocarcinoma and its premalignant lesions. Clin Cancer Res 2006; 12:5423–34.

25. Eberhard A, Kahlert S, Goede V, et al. Heterogeneity of angiogenesis and blood vessel maturation in human tumors: implications for antiangiogenic tumor therapies. Cancer Res 2000;60:1388–93.

26. Stefansson IM, Salvesen HB, Akslen LA. Vascular proliferation is important for clinical progress of endometrial cancer. Cancer Res 2006;66:3303–9.

27. Grunewald M, Avrahum I, Dor Y, et al. VEGF-induced adult neovascularization: recruitment, retention, and role of accessory cells. Cell 2006;124:175–89.

28. Bluel CC, Farzan M, Choe H, et al. The lymphocyte chemoattractant SDF-1 is a ligand for LESTR/fusin and blocks HIV-1 entry. Nature 1996;382: 829–33.

29. Peled A, Petit I, Kollet O, et al. Dependence of human stem cell engraftment and repopulation of NOD/SCID mice on CXCR4. Science 1999;283:845–8.

30. Orimo A, Gupta PB, Sgroi DC, et al. Stromal fibroblasts present in invasive human breast carcinomas promote tumor growth and angiogenesis through elevated SDF-1/CXCL12 secretion. Cell 2005;121: 335–48.

Sensitive detection of *FGFR3* mutations in bladder cancer and urine sediments by peptide nucleic acid-mediated real-time PCR clamping

Makito Miyake [a,g], Kokichi Sugano [a,*], Kiyotaka Kawashima [b], Hiroki Ichikawa [b], Kaoru Hirabayashi [c], Tetsuro Kodama [d,1], Hiroyuki Fujimoto [e], Tadao Kakizoe [e], Yae Kanai [f], Kiyohide Fujimoto [g], Yoshihiko Hirao [g]

[a] *Oncogene Research Unit/Cancer Prevention Unit, Tochigi Cancer Center Research Institute, 4-9-13 Yonan, Utsunomiya, Tochigi 320-0834, Japan*
[b] *Department of Urology, Tochigi Cancer Center Hospital, Tochigi 320-0834, Japan*
[c] *Department of Clinical Laboratory, Tochigi Cancer Center Hospital, Tochigi 320-0834, Japan*
[d] *Tochigi Cancer Center, Tochigi 320-0834, Japan*
[e] *Department of Urology, National Cancer Center Hospital, Tokyo 104-0045, Japan*
[f] *Pathology Division, National Cancer Center Research Institute, Tokyo 104-0045, Japan*
[g] *Department of Urology, Nara Medical University, Nara 634-8521, Japan*

Abstract

Somatic mutations of the fibroblast growth factor receptor 3 (*FGFR3*) gene were detected by peptide nucleic acid (PNA)-mediated real-time PCR clamping. Mutation was detected in negative control containing only wild-type DNA due to a misincorporation of dNTPs to PNA binding sites when the amount of template DNA was decreased to 1 ng. Thus, the amount of template DNA was critical determinant of the assay sensitivity in PNA-mediated PCR clamping. Assay conditions were optimized to detect *FGFR3* mutations in exons 7, 10, and 15, at a concentration of more than 1% mutated DNA using 50 ng of genomic DNA as the template. Mutations were detected in 12 of 13 (92.3%) tumor tissues and 11 of 13 (84.6%) urine samples from patients with superficial bladder cancer, while no mutations were detected in tissues and/or urine samples from patients with muscle-invasive bladder cancer or chronic cystitis.
© 2007 Elsevier Inc. All rights reserved.

Keywords: Superficial bladder cancer; FGFR3; Mutation; Peptide nucleic acid; Real-time PCR

Bladder cancer is one of the most common malignancies worldwide. In the US, bladder cancer is the fourth most common malignancy in men and the ninth in women; there were some 63,210 new cases in 2005 [1]. Urothelial cell carcinoma (UCC) is a histological subtype accounting for more than 90% of all bladder cancers. Bladder UCCs are generally divided into two groups for clinical management, depending on the pathologic stage. The majority of newly diagnosed UCC is superficial disease (pTa or pT1) and patients are treated by transurethral resection (TUR). However, 50–70% of these patients will experience tumor

recurrence and 10–30% will develop muscle-invasive disease (pT2-4) that requires further therapy including cystectomy, chemotherapy or chemoradiotherapy [2]. Cystoscopy is an uncomfortable and invasive examination, but the currently available gold standard for detecting intravesical tumor recurrence. Urine cytology is a noninvasive examination for postoperative management after TUR; however, it is limited by poor sensitivity in cases of low-grade superficial tumors [3].

Recently, mutations of fibroblast growth factor receptor 3 (*FGFR3*) gene have been reported in more than 50% of primary bladder UCC, especially in low-grade and low-stage papillary tumors [2].

Detection of *FGFR3* mutation would be useful for low-grade and low-stage UCCs in urine due to the higher fre-

* Corresponding author. Fax: +81 28 684 5756.
E-mail address: ksugano@tcc.pref.tochigi.jp (K. Sugano).
[1] Director.

quency of this mutation in superficial bladder cancers. Recently, the peptide nucleic acid (PNA)-mediated PCR clamping technique has been developed to improve assay sensitivity for detecting mutations in samples including various tissues, body fluids and stool [4,5]. PNA is a synthetic DNA analog in which the phosphodiester backbone is replaced by a peptide-like repeat of the (2-aminoethyl)-glycine chain [6]. A perfectly matched PNA/DNA hybrid has higher thermal stability than the corresponding DNA/DNA hybrid, hence single base-pair mismatch results in a decrease of Tm at 9–16 °C. On PCR, PNA hybridized with the target sequence can inhibit primer annealing or chain elongation without interfering with reactions of mismatched template DNA; therefore, so-called PNA-mediated PCR clamping induces preferential amplification of mutant DNA fragments even in the presence of an excess amount of wild-type DNA. In the present study, we devised a PNA-mediated real-time PCR clamping technique and established a rapid, simple and sensitive method for detecting *FGFR3* mutations in mutational hotspots in exons 7, 10 and 15 in bladder tumors and voiding urine sediments.

Materials and methods

Samples and DNA extraction. Tumor tissues and preoperative voiding urine samples were obtained from 19 patients with bladder UCC who underwent TUR. Tumors were histologically staged according to the 1997 UICC TNM classification system [7] and graded according to the 1973 WHO classification system [8]. Voiding urine samples from 20 patients with chronic cystitis were assayed as negative controls. Genomic DNA was extracted by proteinase K digestion followed by phenol/chloroform extraction and ethanol precipitation as described previously [9]. Genomic DNA concentrations were determined by ultraviolet measurement with an ND-1000 spectrophotometer (NanoDrop Technologies, Wilmington, DE).

Cell lines. Genomic DNAs extracted from cell lines, UM-UC-14 [10], MGHU3 and J82 were used as assay standards. These cell lines harbored representative *FGFR3* mutations such as homozygous mutation at codon 249 (TCC->TGC) in exon 7 (UM-UC-14), homozygous mutation at codon 375 (TAT->TGT) in exon 10 (MGHU3), and heterozygous mutation at codon 652 (AAG->GAG) in exon 15 (J82), respectively [11,12]. MGHU3 and J82 were generous gifts from Dr. H. LaRue (Laval University Cancer Research Centre, Quebec, Canada) and Dr. Y. Nishiyama (Kyoto University, Kyoto, Japan), respectively.

Primers and PNA for real-time PCR. Primers and PNAs were synthesized by FASMAC. CO., Ltd. (Kanagawa, Japan) and their sequences are listed in Table 1. In exon 7 of *FGFR3*, two types of different point mutations were reported in bladder UCC such as C to T transition at codon 248 substituting cystein for arginine (R248C) and C to G transversion at codon 249 substituting cystein for serine (S249C). PNA was designed as a 15-mer probe which completely matched the bottom strand of the wild-type sequence spanning from the second position of codon 247 through the first position of codon 252 (Fig. 1). Primers and PNAs for exons 10 and 15 were designed according to the same principle as that for exon 7.

PNA-mediated real-time PCR clamping. PNA-mediated real-time PCR clamping was performed with LightCycler (Roche Diagnostics, Mannheim, Germany) in 20 µl reaction volume containing genomic DNA ranging from 50 to 1 ng, 10 µl of QuantiTect PCR master mix (Qiagen, Valencia, CA) containing *Taq* DNA polymerase and SYBR® green I fluorescent dye, 500 nmol/L of each primer and various concentrations of

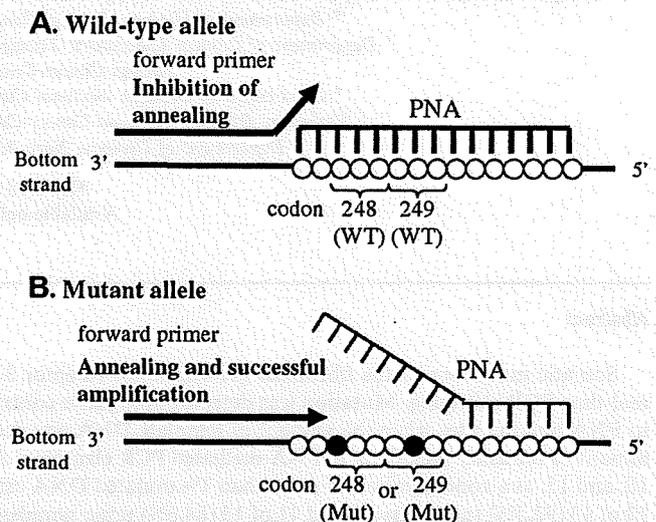**A. Wild-type allele**

B. Mutant allele

Fig. 1. The schematic concept of PNA-mediated PCR in *FGFR3* exon 7. The 15-mer PNA was designed to bind to the bottom strand of wild-type sequence spanning mutational hotspots at codon 248 or 249 in exon 7 of the FGFR3 gene. Forward PCR primer was designed to partially overlap the PNA binding site. A PNA/DNA hybrid with a perfect match suppressed annealing of the forward primer and subsequent amplification of wild-type alleles (A), while a single base pair mismatch of the PNA/DNA hybrid led to decreased thermal stability (ΔT_m 9–16 °C), resulting in preferential amplification of mutant alleles (B).

Table 1
Sequences of primers and PNAs used in this study

FGFR3	Name	Sequences	Product length (bps)	PNA concentration (µM)	PNA binding step (°C)	Annealing step (°C)
Exon 7	7F	5'-TGA GCG TCA TCT GCC CCA CA GAG-3'	182	0.4	72	64
	7R	5'-GGG CCC ACC TTG CTG CCA TTC A-3'				
	PNA-7	H2N-AGC GCT CCC CGC ACC-N2H				
Exon 10	10F	5'-CCA GGC CTC AAC GCC CAT GTC TTT-3'	95	1	67	58
	10R	5'-ACC CCG TAG CTG AGG ATG CCT GCA-3'				
	PNA-10	H2N-CAT ACA CAC TGC CCG C-N2H				
Exon 15	15F	5'-GCA ATG TGC TGG TGA CCG AG-3'	108	2	70	60
	15R	5'-CGG GCT CAC GTT GGT CGT CT-3'				
	PNA-15	H2N-GGT CGT CTT CTT GTA GT-N2H				

Abbreviation: PNA, peptide nucleic acid.

PNAs. Conditions of real-time PCR were as follows; a first denaturing step of 95 °C for 15 min, amplification step of 45 cycles consisting of heat denaturation at 94 °C for 15 s, PNA/wild-type DNA binding step for 5 s, primer annealing step for 20 s and extension step at 72 °C for 20 s followed by a final cooling step of 40 °C for 30 s. The optimized PNA concentrations and reaction temperatures of PNA/WT binding and annealing steps varied for each exon as listed in Table 1. Amplification curves were obtained and the crossing point (CP) was calculated according to fit point method on LCDA (LightCycler Data Analysis)™ software version 3.5. In analysis of clinical samples, genomic DNAs extracted from cell lines were serially diluted with normal genomic DNA at various proportions (100%, 10%, 1%, and 0%) and used as assay standards.

Direct sequencing analysis. Amplified DNA fragments after PNA-mediated real-time PCR clamping were treated by a mixture of exonuclease I and shrimp alkaline phosphatase using ExoSAP-IT (USB Corporation, Cleveland, Ohio) and subjected to a cycle sequencing reaction with a BigDye v3.1 terminator sequencing kit (Applied Biosystems, Foster City, CA) according to the manufacturer's protocol. Sequencing products were purified using a Sephadex G-50 Superfine (Amersham, Uppsala, Sweden) column centrifuge with MultiScreen HV plates (Millipore, Bedford, MA) and subjected to ABI PRISM 3100 Genetic Analyzer.

Results

Validation of assay sensitivity by PNA-mediated real-time PCR clamping using serially diluted assay standards

We evaluated assay sensitivity using DNAs extracted from cell lines harboring *FGFR3* mutations. In the analysis of exon 7, the proportion of UM-UC-14-derived DNA to normal genomic DNA, e.g., tumor cellularity, was adjusted to 100%, 10%, 1%, and 0%. Fifty nanograms of genomic DNA were used as templates for PNA-mediated real-time PCR clamping. The yield of the PCR product was indicated as the intensity of fluorescence emission from SYBR Green I dye bound to double-strand DNA fragments

which increases as the cycle of PCR proceeds (Fig. 2A). The number of cycles reaching a certain level of fluorescence intensity (threshold line) was indicated as the CP. In PCR using templates with different tumor cellularities, CPs were in reverse correlation with tumor cellularities. Direct sequencing of the amplified DNA fragments revealed that the products of 100%, 10%, and 1% standard templates showed a mutation of C to G transversion at codon 249 (TCC->TGC) in exon 7 of *FGFR3* (Fig. 2B). No amplification product was obtained in PCR using distilled water as a negative control, while PCR using wild-type DNA (tumor cellularity: 0%) as the template showed delayed CP, but the amplification profile was similar to mutation-positive samples (Fig. 2A). In direct sequencing of the amplified DNA fragments, no mutation was found at codon 249 while the background signal within the PNA-binding region was increasing (Fig. 2B). This phenomenon implied that PNA-mediated PCR clamping facilitated the misincorporation of nucleotides to the PNA binding site in the absence of *FGFR3* mutations in the template.

Assay sensitivity of PNA-mediated real-time PCR clamping is defined by the amount of template DNA, the decrease of which induced misincorporation of dNTPs to PNA binding sites

Further experiments were carried out to validate assay conditions to reduce the rate of misincorporation and improve assay specificity. Assay standards with tumor cellularities ranging from 100%, 10%, 1%, and 0% were amplified in octaplicate samples ($n = 8$) by PNA-mediated real-time PCR clamping. Amounts of template DNA were
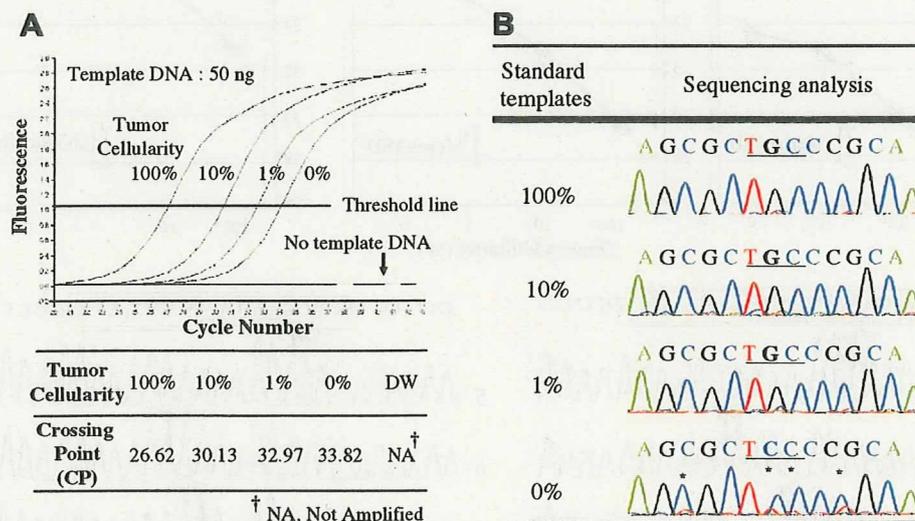

Fig. 2. Amplification of serially diluted standard templates by PNA-mediated real-time PCR clamping in *FGFR3* exon 7. Genomic DNA harboring a homozygous S249C mutation was serially diluted with wild-type DNA. Concentrations of mutated DNA in the sample were adjusted as follows: 100%, 10%, 1%, and 0%. (A) Fifty nanograms of template DNA were amplified using PNA-mediated real-time PCR clamping. The crossing points obtained by the threshold line at the fluorescence level of 1.0 were 26.62, 30.13, 32.97 and 33.83, respectively. (B) Subsequent DNA sequencing analysis revealed that PCR fragments of 100%, 10%, and 1% standard showed TCC to TGC mutations at codon 249, whereas that of 0% standard showed wild-type sequence, while background signals increased in the sequencing profile. Underlined letters indicate codon 249. Asterisks indicate the increase of background signals.

changed in each run from 50 ng, 10 ng to 1 ng. Amplification profiles and CPs of the assay were compared between

runs (Fig. 3A and B). In the condition using 50 ng of genomic DNA as the template, CVs of the CPs were relatively
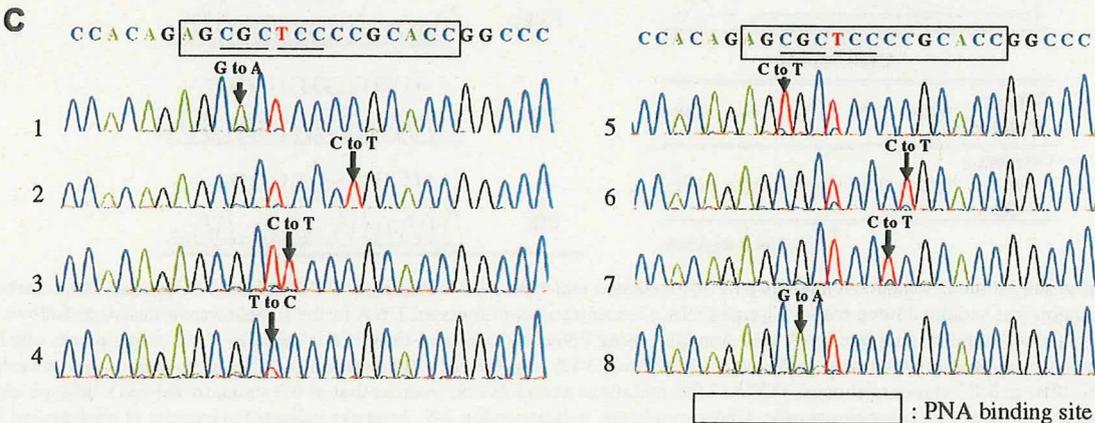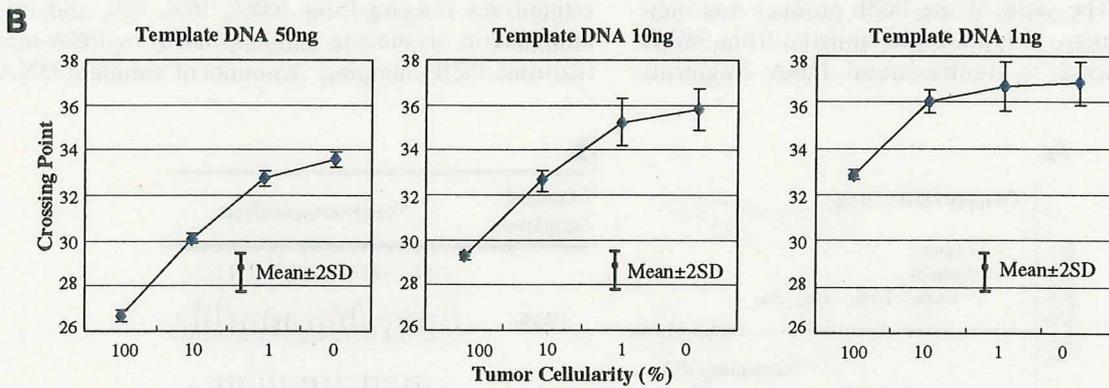
A

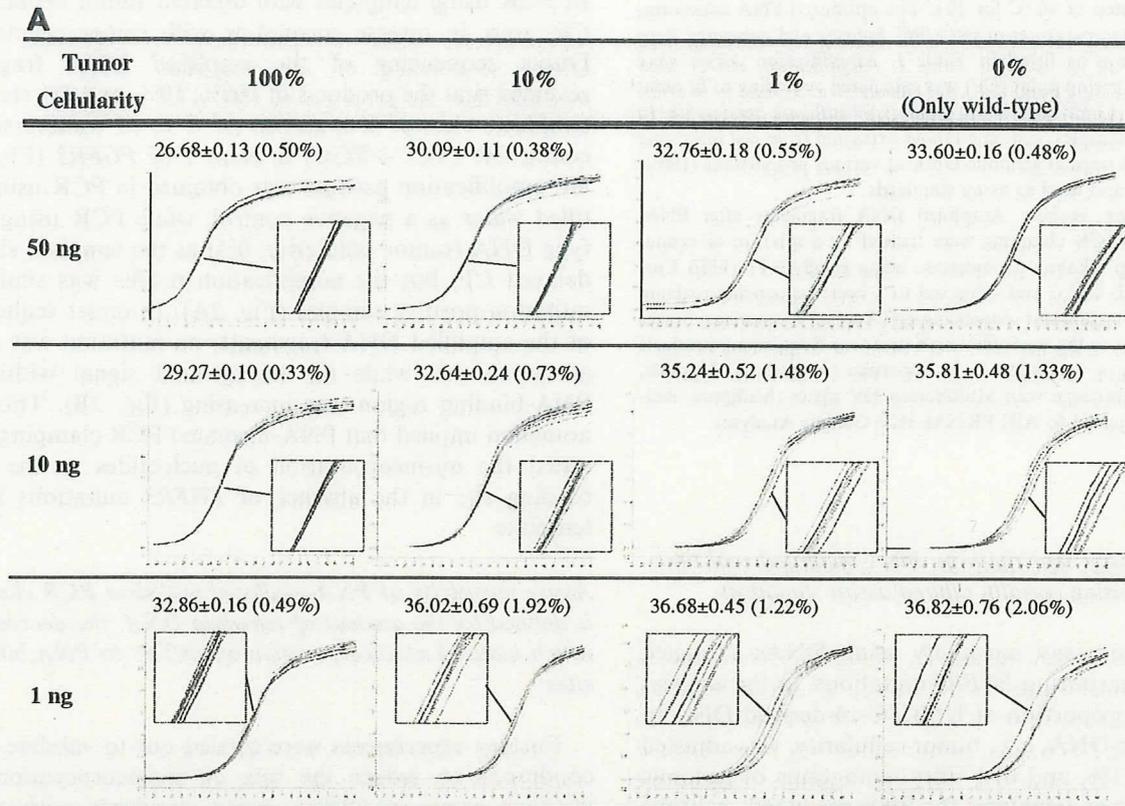| Tumor Cellularity	100%	10%	1%	0% (Only wild-type)
50 ng	26.68±0.13 (0.50%)	30.09±0.11 (0.38%)	32.76±0.18 (0.55%)	33.60±0.16 (0.48%)
10 ng	29.27±0.10 (0.33%)	32.64±0.24 (0.73%)	35.24±0.52 (1.48%)	35.81±0.48 (1.33%)
1 ng	32.86±0.16 (0.49%)	36.02±0.69 (1.92%)	36.68±0.45 (1.22%)	36.82±0.76 (2.06%)

B

C

: PNA binding site

Table 2
Summary of patients' tumor histology, urine cytology and *FGFR3* mutations in tumor tissues and urine sediments

Case No.	Tumor stage/Histological grade	Urine cytology	*FGFR3* mutation status (Tumor cellularity (%))					
			Tumor tissues			Urine sediments		
			Ex 7	Ex 10	Ex 15	Ex 7	Ex 10	Ex 15
1	pTa/G1	Negative	S249C (34.2)	Y375C (100)	WT	S249C (2.4)	WT	WT
2	pTa/G1	Negative	WT	Y375C (100)	WT	WT	Y375C (2.1)	WT
3	pTa/G1	Atypia	S249C (92.4)	WT	WT	S249C (42.1)	WT	WT
4	pTa/G1	Negative	S249C (55.2)	WT	WT	S249C (2.4)	WT	WT
5	pTa/G1	Negative	WT	Y375C (100)	WT	WT	Y375C (100)	WT
6	pTa/G2	Positive	WT	WT	WT	WT	WT	WT
7	pTa/G2	Atypia	S249C (45.0)	WT	WT	S249C (5.5)	WT	WT
8	pTa/G2	Atypia	WT	Y375C (19.0)	WT	WT	Y375C (34.5)	WT
9	pTa/G2	Atypia	WT	Y375C (6.5)	WT	WT	Y375C (3.8)	WT
10	pT1/G2	Negative	S249C (44.1)	WT	WT	WT	WT	WT
11	pT1/G2	Positive	S249C (67.2)	WT	WT	S249C (51.9)	WT	WT
12	pT1/G2	Negative	S249C (34.6)	WT	WT	S249C (6.8)	WT	WT
13	pT1/G3	Negative	S249C (51.6)	WT	WT	S249C (10.5)	WT	WT

Abbreviations: NE, not examined; ND, not determined; WT, wild-type.

uniform regardless of tumor cellularities, while they increased with the reduction of tumor cellularities and were inversely correlated with the amounts of template DNAs in analysis using 1 ng of genomic DNA as the templates (Fig. 3A).

The association between tumor cellularity and CPs was compared in analyses using 50, 10 and 1 ng as template DNAs ($n = 8$) (Fig. 3B). In analysis using 50 ng of genomic DNA as templates, CPs were significantly different among tumor cellularities ranging from 100%, 10%, 1%, and 0%. In contrast, there was no significance of CPs between 1% and 0% in analysis using 10 ng of genomic DNA as templates and between 10% and 1% or less in analysis using 1 ng of genomic DNA as templates. These results indicated that 50 ng of template DNA was required for the reproducible detection of *FGFR3* mutation at a concentration of 1%, i.e., 100-fold excess amount of wild-type DNA.

Sequencing analyses of amplified DNA fragments at various concentrations were performed and those using 1 ng of template DNAs containing only wild-type DNA showed that all samples had point mutations within the PNA binding sites (Fig. 3C). Mutations seemed to occur at random and in different positions from previously reported mutational hotspots, suggesting that these mutations were artifacts induced by PNA-mediated PCR clamping.

Similar approaches were adapted to construct assay protocols to detect mutations in exons 10 and 15. Genomic DNAs extracted from MGHU3 and J82 were diluted with wild-type genomic DNA and prepared as assay standards for exons 10 and 15, respectively, and assay sensitivities for detecting mutations $\geqslant 1\%$ cellularities were validated in control experiments (data not shown).

Detection of FGFR3 mutations in tissues of bladder cancer and corresponding urine sediments

Mutations of *FGFR3* were detected using the above-mentioned assay conditions in tissues and urine sediments from 13 patients with superficial bladder cancer (pTa stage, 9 cases; pT1 stage, 4 cases) and 6 cases of invasive bladder cancer ($\geqslant$pT2 stage, all cases). In analysis of 13 cases with superficial bladder cancer, *FGFR3* mutations and estimated tumor cellularities in exons 7, 10, and 15 were summarized in Table 2. We defined the CP of the assay standard corresponding to 1% cellularity as a minimal detectable dose for *FGFR3* mutations; therefore, a sample showing a CP less than that of 1% standard on each run was determined to be positive for mutation. *FGFR3* mutations in exon 7 were detected in 8 of 13 (61.5%) superficial bladder cancer tissues and sequencing analyses confirmed that all cases harbored S249C mutation in exon 7 of *FGFR3*. The mean tumor cellularity of mutation-positive cases was 53.0% ($n = 8$, range 34.2–92.4%). In the analysis of urine sediments, S249C mutation was detected in 7 out of 8 cases (87.5%) harboring S249C mutation in primary tumors.

Fig. 3. Variations of crossing points (CPs) defined by tumor cellularities and amounts of template DNA. Fifty nanograms, 10 and 1 ng of standard templates with tumor cellularities ranging from 100%, 10%, 1%, and 0% were subjected to PNA-mediated real-time PCR clamping in octaplicated samples ($n = 8$). (A) CPs are indicated as the mean ± SD (CV%) in each run. Observed CV% was maximal in the analysis of 0% standard (only wild-type DNA) using 1 ng of DNA as the template. Insets magnify variations of amplification curves in the log-linear phase. (B) Tumor cellularities and CPs in 50 ng, 10 ng, and 1 ng of the template DNAs were plotted onto a line graph, in which error bars indicate the mean ± 2SD of CPs in each template DNA quantity. (C) Direct sequencing of DNA fragments amplified by PNA-mediated real-time PCR clamping using 1 ng of template containing only wild-type DNA. The uppermost sequence represents the wild-type sequence. The 15-mer sequence surrounded by a rectangle represents the PNA binding site. Codons 248 and 249 are underlined. Sequencing analysis revealed that the 8 amplicons present various types of mutagenized sequences within the PNA binding site. Black arrow indicates the site of point mutation in each sample.

The mean tumor cellularity of urine sediments was 17.4% ($n = 7$, range 2.4–51.9%). Likewise, FGFR3 mutations in exon 10 were detected in 5 of 13 (38.5%) tumor tissues of superficial bladder cancer and all cases harbored Y375C mutation. In analysis of urine sediments, Y375C mutation was detected in 4 of 5 cases (80%) harboring Y375C mutation in the primary tumor (Table 2). The mean tumor cellularity of mutation-positive cases was 63.1% ($n = 5$, range 6.5–100%) in tumor tissues and 35.1% ($n = 4$, range 2.1–100%) in urine sediments, respectively. No mutations were detected in exon 15 of FGFR3 either in tissues or urine sediments (Table 2). In the analysis of muscle-invasive bladder cancer ($n = 6$) and 20 urine samples from patients with chronic cystitis, FGFR3 mutations were not detected either in tumor tissues or urine sediments (data not shown).

Taken together, FGFR3 mutations in superficial bladder cancer were detected in 12 of 13 (92.3%) tumor tissues and, in analysis of urine sediments, 11 (91.7%, except case no. 10) of 12 cases harboring mutations in primary tumor. One case (no. 1) showed multiple mutations comprising S249C in exon 7 and Y375C in exon 10 in tumor tissue, but only S249C in exon 7 was detected in the urine sample.

Discussion

The present study is the first report of the PNA-mediated real-time PCR clamping technique for detecting FGFR3 mutation. The assay can be performed by a simple one-step reaction in a single tube using SYBR® green I fluorescent dye. PNA-mediated real-time PCR clamping screens for the presence or absence of mutations; however, PCR products can be easily subjected to direct sequencing to identify the type of mutation.

The amounts of genomic DNA extractable from urine sediments are often trace, particularly in patients during follow-up after TUR or with a small tumor burden; therefore, the method for detecting mutations should be sensitive and specific enough using a small amount of genomic DNA as the template. We validated that this assay enabled reproducible and reliable detection of mutations in a 100-fold excess amount of wild-type DNA using 50 ng of genomic DNA as the template, while it did not work well when the amount of template DNA was less than 10 ng due to the increase of assay CVs. In analysis using 1 ng of genomic DNA as the template, CPs of 1% or 10% standard was indistinguishable from that of 0% standard. CVs of CPs increased in reverse proportion to the decreasing amount of template DNA. In direct sequencing, all PCR products of 0% standard (wild type) amplified from 1 ng of template DNA showed mutations in PNA binding sites (Fig. 3C). Such mutations seemed to occur at random and this phenomenon may account for the increase of CVs of CPs in the experiment using a smaller amount of template DNA. In PCR, changes in the nucleotide sequence are attributable to errors made by DNA polymerase [13]. One nanogram of genomic DNA corresponds to 300 copies of genomic DNA and the length of the PCR product for exon 7 is 182 bps. Numbers of nucleotides in the target DNA are 5.46×10^4 and random errors will not interfere with subsequent analyses in conventional PCR, considering the fidelity (error rate per nucleotide) of Taq DNA polymerase is from $\sim 2 \times 10^{-4}$ to $<1 \times 10^{-5}$ bps, however, PNA bound to wild-type sequences suppressed the amplification of template DNA. As a result, only part of the template DNA was available for PCR, and DNA fragments carrying misincorporated dNTPs would be amplified selectively. This phenomenon seems to be a limiting factor to define assay sensitivity in PNA-mediated real-time PCR clamping.

Thus, we optimized assay conditions to detect FGFR3 mutations in exons 7, 10, and 15 in a 100-fold excess amount of wild-type DNA. In analysis using clinical samples, FGFR3 mutations were detected in 92.3% (12/13) of superficial bladder cancer and no mutations were detected in muscle-invasive bladder cancer (0/6) or urine sediments of chronic cystitis (0/20). FGFR3 mutations were detected in 91.7% (11/12) of urine sediments of which primary tumors presented FGFR3 mutations. The types of mutations detected in urine sediments coincided with those of tumor tissues, except for one case (Case no. 1) with double mutations in exon 7 and exon 10, with urine sediments showing only a mutation in exon 7 of the FGFR3 gene. Our results suggested that this assay was highly sensitive and specific for detecting FGFR3 mutations in urine samples.

Sensitive detection of FGFR3 mutations in urine samples would be beneficial for monitoring tumor recurrence of superficial bladder cancer and would also be suitable as a favorable prognostic indicator in predicting the minimal risk of their progression to muscle-invasive bladder cancer. Further study is ongoing to elucidate the significance of FGFR3 mutations detectable in urine samples in the clinical management of bladder UCC.

Acknowledgments

References

[1] American Cancer Society Cancer Facts and Figures 2005, American Cancer Society, Atalanta, 2005.
[2] K. Sugano, T. Kakizoe, Genetic alterations in bladder cancer and their clinical applications in molecular tumor staging, Nat. Clin. Pract. Urol. 3 (2006) 642–652.
[3] H.G. Wiener, C. Mian, A. Haitel, A. Pycha, G. Schatzl, M. Marberger, Can urine diagnostic tests replace cystoscopy in the management of bladder cancer? J. Urol. 159 (1998) 1876–1880.
[4] L. Prix, P. Uciechowski, B. Böckmann, M. Giesing, A.J. Schuetz, Diagnostic biochip array for fast and sensitive detection of K-ras mutations in stool, Clin. Chem. 48 (2002) 428–435.